RECEIVED BY TIC SEP 19 1975

PREPRINT UCRL-77213

Conf-750970--1

Lawrence Livermore Laboratory

ELECTRON-BEAM PUMPING OF VISIBLE AND ULTRAVIOLET GAS LASERS

Laird P. Bradley

September 12, 1975

This paper was prepared for submittal to the proceedings of the summer school on the Physics and Technology of High Power Gas Lasers, *International College on Applied Physics*, Capri, Italy, September 22-October 4, 1975.

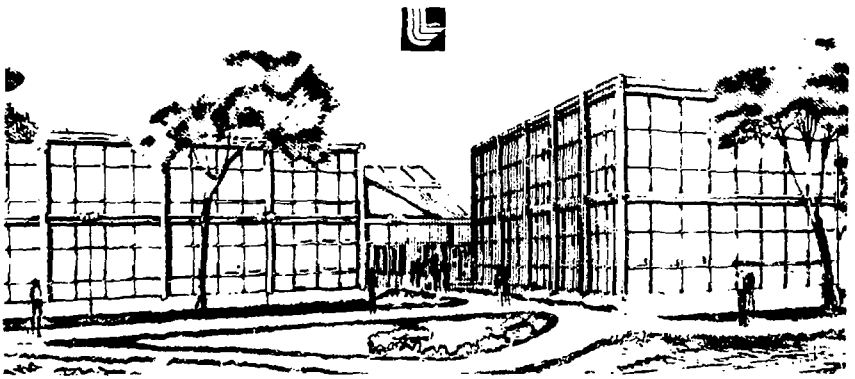

ELECTRON-BEAM PUMPING OF VISIBLE AND ULTRAVIOLET GAS LASERS*

Laird P. Bradley

Lawrence Livermore Laboratory, University of California

Livermore, California 94550

Abstract

Several techniques for using direct electron-pumping of gas lasers are reviewed. The primary objective is to categorize pump geometries and to give guidelines for gun selection and pulser design. Examples and application of pump technology are given.

* This work was performed under the auspices of the U.S. Energy Research & Development Administration.

INTRODUCTION

Inertial confinement for fusion (1) requires visible or near ultraviolet lasers at high peak power for optical coupling of the radiation to the pellet plasma (2). A lower wavelength bound is set by two photon absorption in the laser and optical elements (3). Uranium isotope separation (4) also requires such lasers at high average power. Since uranium has an ionization potential of ~6 eV, at least one photon of any multiphoton isotopic separation process will probably fall within this wavelength regime (5).

These applications, among others, require energetic, efficient, and reliable lasers which, unfortunately, do not currently exist. The problem of identifying and selecting potentially efficient laser transitions has been discussed by Rhodes (6), Murray (7), Judd (8), and others. I will describe the techniques and technology of electron-beam pumping of potentially attractive candidate lasers for the aforementioned applications. As examples of such candidates I will use KrO (9) for high peak-power applications, and N_2^+ (10) for high average power. These examples are presented as "problems for the students" because these lasers are undergoing active investigation with an increasing data base developing, and because there are many options and trade-offs available to consider. I will touch upon e beam sustainer pumping technology where there is relevant overlap.

The visible transitions in $O(^1S_0) - O(^1D_2)$ at 5577 Å and $N_2^+(B^2\Sigma_u^+) \rightarrow N_2^+(X^2\Sigma_g^+)$ at 4278 Å have been observable since prehistory in the form of auroral displays (11) in the polar regions of the Earth. Such aurora are driven by intense electron currents (12) coupled from the solar corona and channeled through the Earth, and interplanetary magnetic fields into the Earth's atmosphere. The range of the ≲40-keV electrons as they enter an increasing atmospheric density causes peak deposition in the E region ≳90 km, where atomic oxygen and molecular nitrogen are dominant (13). Ground-base spectral observation of an artificial aurora (14) produced by a rocket-borne e-beam gun shows significant peaks in the visible only at 5577 and 4278 Å as shown in Fig. 1.

It is extremely interesting and perhaps more than coincidental that these transitions, which are driven in nature by e beams, have recently been made to lase in the laboratory using e-beam pumping. With e-beam excitation Murray et al. (15) have utilized an in-situ pumping from a rare gas dimer to produce an inversion in atomic oxygen. Collins and Cunningham (16) have used charge transfer from the helium driver to produce excitation of the molecular nitrogen ion. Illustrations of the natural auroral and laboratory laser emissions are shown in Fig. 2. These lasers are but the first of new classes of potentially attractive visible lasers.

PUMP CONFIGURATIONS

Laboratory sources of intense e beams (up to 1 MJ (17)) are available for preliminary pumping experiments. Most existing sources, however, were optimized for the simulation of nuclear weapons effects (18) or for other plasma experiments (19). The source technology is undergoing significant changes to configure e beams for laser pumping.

In general, the laboratory e beam for laser pumping is generated by high voltage applied across a vacuum or low-pressure diode or grid tube. The accelerated electrons pass through thin foil into the gas-filled laser cavity. Depending upon the laser transition and plasma characteristics, either the primary or secondary electrons, or both, may play the dominant role in pumping.

Most recent experiments have utilized a transverse pump configuration (20) with the e beam orthogonal to the laser beam as shown in Fig. 3. Generally this one-sided pumping is inefficient because of electron scatter out of the cell and nonuniform e-beam deposition across the cell (21). Two geometries more attractive for direct transverse e-beam pumping are the cylinder and the two-sided slabs illustrated in Fig. 4. In these configurations greater than 50% of the available electron energy can be delivered uniformly to the cavity. These geometries are suitable for pumping high pressure gas where the electron range is relatively short.

An e beam injected into a gas with a bias electric field, as used in CO_2 (22) and shown in Fig. 5, may find application for visible transition lasers by using a more intense e beam and by applying a higher E/p bias. The e beam is used in this mode to provide significant initial plasma density and hence conductivity, to control the uniformity of the high E/p discharge minimizing the possibility of streamers and arcs, and to supply electrons lost to the discharge.

Axial e-beam pumping (with the e beam and laser parallel) with an intense magnetic field B_z provides an alternative geometry for pumping as shown in Fig. 6, whereas transverse pumping is most effective for high-pressure gases ($\gtrsim$1 atm). The axial configuration may be used to pressures of $\lesssim$1 atm as determined by the relative range of the electrons. Generally the magnetic field is made sufficiently intense so that its containment effect reduces the side scatter of electrons from the beam.

The axial geometry permits other, although not necessarily efficient, means of pumping lower pressure gas. If we envision a cylindrical e beam propagating through gas in a closely spaced conducting pipe, then as the current increases during the beam rise time, an electric field is induced in the gas according to Faraday's law. This electric field drives an avalanche of the background electrons. This mechanism applies an axial E/p to the gas and the results are analogous to that in a standard-pulsed two-electrode discharge. The accelerating voltage is only relevant to penetrating a reasonable volume of gas.

For example, in an early e-beam pumped nitrogen-laser experiment, Dreyfus and Hodgson (23) axially applied a 12 kA (I_p) e beam with a rise time of $\sim$1.5 ns (τ_r) to $\sim$30 Torr of N_2 as shown in Fig. 7. According to Faraday's law, the axial electric field is $E_z = -10^{-5}\, I_p/\tau_r \simeq 710^3$ V/cm. Thus, E/p $\simeq$ 200 V/cm·Torr, the initial optimum E/p for pumping a $N_2(C) \rightarrow N_2(B)$ at 5371-Å laser (24). In fact Davies (25) used an axial discharge tube with about the same E/p and obtained roughly the same output power. McArthur and Poukey (26) have shown this induced field to be dominant in the e-beam N_2 laser, as opposed to the cascade scheme originally suggested by Dreyfus and Hodgson.

When an intense e beam propagates through a low-pressure gas ≤1 Torr, conditions are ripe for the development of a variety of beam-plasma instabilities. Fainberg and co-workers [27] have used the two-stream instability to pump an Ar^+ laser. In the configuration shown in Fig. 8, they injected a ∿30-keV, 30-A, and 40-μs axial e beam into a gas at 10^{-3} Torr. The e beam preionized the gas. The directed primary beam energy converted through the electrostatic two-stream instability to electron plasma waves, damped through electron-neutral collisions, and thereby heated the background electrons to ∿90 eV. Such high-electron temperatures produced significant ionization and, hence, pumping of the argon-ion laser transitions. They obtained ∿100 W for 30 μs on the $Ar^+(3p^44p) \rightarrow Ar^+(3p^5) + h\nu(4480\ \text{Å})$ transition.

The two stream or other instabilities might have several attributes. They might shape the secondary electron-distribution function to preferentially excite a particular electronic state and perhaps control the tail of the distribution to enhance or suppress ionization. These instabilities might be used to foreshorten the range of electrons, thereby more efficiently coupling energy into the plasma. Fainberg et al. have shown that one can also preferentially control the ion-distribution function to reduce the effect of radiation trapping.

PUMP MECHANISMS

The relativistic e beam and its cascade of secondaries are quite efficient in producing ionization and exciting highlying electronic levels. In this section we categorize several mechanisms by which this ionization and excitation may be channeled to preferentially produce a population inversion.

Pump Mechanisms Using Ionization

Ion laser. In the ion laser referred to earlier, Fainberg et al. [27] distinguish two regimes. In a pulsed regime a group of hot electrons (about a few hundred electron volts) cause direct ionization

$$Ar + e \rightarrow Ar^+(3p^44p) + 2e. \tag{1}$$

In a quasistationary regime with cooler electrons (∿10-15 eV) direct ionization is unlikely and a two-step process occurs:

$$e + Ar(3p^6) \rightarrow Ar^+(3p^5) + 2e, \tag{2}$$

$$e + Ar^+(3p^5) \rightarrow Ar^+(3p^44p) + e. \tag{3}$$

In the direct process the upper and lower laser levels are equally excited and inversion occurs because of radiative decay of the lower level. In the two-step process at lower electron temperatures, the upper state is preferentially pumped.

Rare gas dimer laser. The rare gas dimer laser (6) utilizes both primary and secondary electrons to pump a bound state, with the laser transition occurring between a bound Rydburg excited state and an unbound ground state as follows:

$$e + Ar \rightarrow Ar^* + e, \tag{4}$$

$$Ar^* + 2Ar \rightarrow Ar_2^* + Ar, \tag{5}$$

and

$$e + Ar \rightarrow Ar^+ + 2e, \tag{6}$$

$$Ar^+ + 2Ar \rightarrow Ar_2^+ + Ar, \tag{7}$$

$$e + Ar_2^+ \rightarrow Ar^* + Ar, \tag{8}$$

$$Ar^* + 2Ar \rightarrow Ar_2^* + Ar, \tag{9}$$

thus

$$Ar_2^* \rightarrow 2Ar + h\nu(1265\ \text{Å}). \tag{10}$$

Such excimer emission occurs for all the rare gases over a bandwidth ~100 Å centered at 1265 Å for Ar_2^*, 1460 Å for Kr_2^*, and 1720 Å for Xe_2^*. The asterisk designates the metastable rare-gas state ($^3P_2$) and to some degree higher lying electronic levels that are collisionally channeled at high pressure to the lowest lying state.

Dimer collisional losses exemplified by the Penning process

$$2\ Ar_2^* \rightarrow Ar_2^+ + 2Ar + e, \tag{11}$$

$$\rightarrow Ar^+ + 3Ar + e,$$

tend to reduce the net efficiency of uv fluorescense. With a reduced excited-state density, efficiencies approaching 40% might be obtained. Recently Turner, Taska, and Hoff (28) obtained an excimer fluorescence efficiency of ~30% by using a low-current density, long-pulse e-beam pump (200 kV, 5 A/cm^2, 1 μs).

Charge transfer laser. Another recent development is the e-beam pumped charge-transfer laser. Collins and Cunningham (29) have used the near-resonant charge transfer of $He_2^+ + N_2 \rightarrow N_2^+(B^2\Sigma_u^+) + 2He$ leading to the lasing transition $N_2^+(B^2\Sigma_u^+) \rightarrow N_2^+(X^2\Sigma_g^+) + h\nu$. In essence the e-beam energy is stored (for very short periods) in the charged states of He_2^+ and collisionally transferred to N_2^+. Gain has been observed on the (0,0), (0,1), and (0,2) vibrational levels at 3914, 4278, and 4709 Å. The experiments used a 1-MV e beam in a transverse geometry at 1.4 kA/cm^2 and 20-ns full width half maximum (FWHM). A few torr (~10) of N_2 were mixed into 2 atm of helium. Under these conditions most of the e-beam energy passed through the gas depositing only 0.014 J/cm^3 in the gas. Based on this energy density, a cavity volume of 0.63 cm^3, a measured laser output, an efficiency (η_ℓ) of ~2% was determined.

It is important to note that most efficiencies are reported (as is this one) in terms of e-beam energy deposited in the gas. The net gun-to-laser efficiency above is only ~10^{-3}%. We will demonstrate later in this paper that one might obtain total efficiencies approaching 1% for the above example by proper injection techniques.

Powell, Murray, and Rhodes (9) have recently demonstrated that the rare gas dimer excitation may be transferred to oxygen to produce an inversion in atomic oxygen. Two processes are relevant as described in the next two paragraphs.

In several atmospheres of krypton with an admixture of a few torr of oxygen, a collisional process between the rare-gas dimer and ground-state oxygen is probably (this is not unambiguously determined) the dominant mechanism for producing an inversion (30):

$$Kr_2^* + O_2 \rightarrow 2\,O + 2Kr,$$

$$Kr_2^* + O(^3P) \rightarrow O(^1S) + 2Kr. \qquad (12)$$

The above mentioned authors have obtained lasing on the weakly bound $O(^1S_0)$ of the excimer KrO (and similarly for ArO_0 and XeO) giving emission essentially on the atomic line center at 5577 Å. They used a transverse excitation configuration of a 1-MeV e-beam generator to provide pump-energy densities of ~1 J/cm^2 and have obtained 10 mJ of laser energy from a 10-cm-long cell. It should be noted that although $O(^1S)$ makes a poor oscillator because of the low gain, it is ideally suited to make a power amplifier precisely because of its low-gain at high-energy storage. It should also be noted that a broadband absorption occurs during e-beam pumping (9). This absorption might be useful in reducing the parasitic oscillation problem prior to energy extraction in the amplifier mode.

An alternate mechanism for the use of efficiently produced rare-gas fluorescence is to photolytically transfer this energy. Powell and Murray (31) as well as Hughs (32) have used e-beam pumped argon-dimer laser radiation and fluorescence respectively as shown in Fig. 9, to photodissociate the N_2O contained in a contiguous cell and separated by MgF$_2$ windows. Gain has been observed by Hughs et al. in the $O(^1S)$ thus produced. Intensive work is underway at several laboratories to conduct energy extraction experiments and to more fully evaluate the potential of this system (or associated systems as $S(^1S_0)$) as a candidate for laser-fusion applications.

Pumping by Collisional Transfer

We have already mentioned collisional transfer processes in the foregoing examples. The Ar-N_2 laser is pumped primarily by collisional transfer from Ar* providing preferential pumping of the $N_2(C^3\Pi_u) \rightarrow N_2(B^3\Pi_g)$ transition. Lasing has been observed on the (0-2), (0-1), and (0-0) vibrational levels at 3805, 3577, and 3371 Å.

Searles (33), Collins (16), Hunter (34), Basov (35), and Ault (36) have separately examined this system using transverse pumping. Recently Ault (37) used a small system with cylindrical injection. The efficiencies reported vary from ≲0.4 to 3%.

Chemical laser. Gerber and co-workers have recently obtained energetic infrared pulses with E-beam initiation of chemical reactions in H_2-F_2 (38). The energetic electrons cause dissociation of F_2 and the following chain reaction

$$I + H_2 \rightarrow HI^* + H, \tag{13}$$

$$H + I_2 \rightarrow HI^* + I. \tag{14}$$

They employed an axial e-beam configuration with a 2-MV, 3[illegible]-kA, [illegible]-ns e beam. The electrical efficiency was [illegible]% and the chemical efficiency was [illegible]%. Problems associated with long wavelength, pulse width, parasitics, and beam quality must be considered before this laser can be considered a candidate for fusion.

Other Pump Mechanisms

Laser action has been reported in GaAs (39) and in CdS (40) solids pumped by electron beams typically [illegible]1-20 A/cm^2. It is possible that arrays of such lasers (41) might produce high-average powers.

Although there are these and many other interesting possibilities such as e-beam pumped vapor-dye lasers (42), we restrict the discussion to the e-beam pumping of some selectively demonstrated visible-gas lasers.

SOURCE PARAMETER DETERMINATION

Although we are faced with orders of magnitude of variation of most parameters such as voltage, current density, pulse width, pressure and gas particle mass, we (43) can quickly narrow the parameter space to establish a reasonable set of working parameters to aid in further discussions.

Gun Voltage Determination

The value of the individual electron kinetic energy plays a minor role in the pumping kinetics. This is because the electron cross section is a smooth, slowly varying function for energy between 10^7 and 10^8 eV. The gun voltage, therefore, is determined by practical considerations. It must be high enough so that the electrons efficiently penetrate the foil separating the gun and the gas. (One can use lower voltage guns with differential pumping (44) or even use the diode plasma as the laser medium (45), but such schemes have not found wide applications.) Thus we are restricted to voltages $\geq$200 kV. At the higher voltages one must cope with x-ray production. X-ray production affects system efficiency; for example, a 10-MeV beam-pumping xenon looses 25% of its energy to x rays. X rays also impact system cost because shielding is necessary to protect humans and to protect diagnostics, the latter presenting the most severe constraint in an experimental situation. The prime consideration in determining gun voltage is that the electrons must be sufficiently energetic to uniformly pump the gas cavity of interest. The practical working-gun voltage is therefore $0.2 \leq E \leq 5$ MV.

The cell dimension parallel to the E beam is related to the gun voltage as follows. The electron range R_0 in gas without externally applied electric or magnetic fields is given by

$$R_0 = \frac{0.4V}{\left.\frac{dE}{dX}\right|_{BS}^{E}}, \tag{15}$$

where ρ is gas density and $(dE/dX)_{BS}$ is the deposition function given approximately by (46)

$$\left.\frac{dE}{dX}\right|_{BS} \approx 2 \text{ MeV}/(\text{gm/cm}^2). \tag{16}$$

A more accurate value may be obtained from the Berger and Seltzer tables (47), but the objective herein is to develop a set of guidelines for system design. Any particular cavity will require full three-dimensional simulation by a numerical code such as SANDYL (48), or extensive experimental variations to select optimum conditions.

The cell transverse dimension w is set at some fraction F of the electron range depending on the desired pump uniformity:

$$w = F R_0 \tag{17}$$

where $0 < F < 1$. F is determined from SANDYL calculations such that the superimposition of oppositely directed beams provides a net uniform deposition as shown in Fig. 9. Generally F is approximately 0.4 and might be selected as 0.3 for a slab cell or 0.5 for a cylindrical cell, although it depends in detail on the particular gas. We select a value of F = 0.4 and obtain the rule of thumb (45) that

$$\lambda = \zeta w_{cell}, \tag{18}$$

where λ = MW, w_{cell} = cm, and $\zeta \approx 4 \times 10^{-3}$ MW, with M in amu and P in atm.

Determination of Gun Current Density and Pulse Width

The current density J injected into the cell and pulse width Δt are determined jointly by kinetics and by practical considerations. A second rule of thumb (45) is that

$$J\Delta t = \frac{E_{Ve}}{\zeta}, \tag{19}$$

where J is in A/cm^2, Δt in μs, and E_{Ve} is the deposited electron-energy density in J/cm^3.

The current density is limited by foil heating, deformation, rupture, and fatigue. From empirical data and particular calculations (49,50), for short-pulse single-shot operations, one can use $J \lesssim 1$ kA/cm^2 and for continuous operation one can use $J < 1$ mA/cm^2 for most practical foils. The foils typically used are aluminum, titanium, kapton with screen, and stainless steel with thickness ~0.002 cm.

A constraint on the maximum deposited e-beam energy density is eventually the maximum light flux that can be extracted through an amplifier window, the latter being $\varepsilon_\ell \lesssim 5$-10 J/cm^2 for short visible pulses (51).

If significant energy density is deposited by the electrons, then an overpressure is produced by gas heating limiting the ratio of E_{Ve} to pressure,

$$I_{Ve}/P \lesssim \quad (20)$$

for pulsed operation (45).

In general for practical-pulsed amplifiers, one may infer the following operating regime:

$$E_{Ve} \lesssim 1\text{-}5\ J/cm^3,$$

$$0.2 \lesssim V \lesssim 5\ MV,$$

$$J \lesssim 50\text{-}200\ A/cm^2,$$

$$\Delta t \gtrsim 10\text{-}100\ ns. \quad (21)$$

Although these are not fixed bounds, they tend to serve as guidelines for system design considerations. We will return to these relationships and show how they apply in the design of particular amplifier modules.

Determination of Injected Electron Angles

Another very important parameter is the initial electron trajectory direction at the cell wall. The net local beam direction is called divergence and the mean spread about this direction is called emittance. The origin and effect of these parameters will be discussed in the sections on diodes and deposition.

ELECTRON BEAM DEPOSITION IN GAS

Although a full three-dimensional code is required to analyze electron energy loss to a gas, we can intuitively understand this process by considering the deposition of a narrow pencil of electrons directed into a gas with various foil and wall locations, by evaluating the effects of applied electric and magnetic fields if relevant, and then by considering a general cell geometry as a superimposition of such beamlets. Such an approach is possible because the beam-electron density is significantly less than the gas density for many cases of interest and the interaction is primarily between electrons and gas atoms.

In traversing the gas, an electron undergoes many small angle scatterings caused by the spatial variation of the gas-atoms electric fields along the path. Occasionally it approaches an atom close enough to undergo a large-angle deflection or to interact with the extranuclear electronic structure of the atom causing an energy loss to the electron. This results in excitation and/or ionization of the target atom. In essence, the electron follows a zigzag path through the gas and deposits energy microscopically continuously along its path.

Considering a narrow pencil beamlet of electrons incident on a semi-infinite region of gas, these processes give rise to an initially straight region of deposited energy followed by a wide expansion as shown in Fig. 10. The isodensity deposition contours have a shape similar to a light bulb. Some fraction of the electrons are backscattered away from the gas. If a tube was accelerating the electrons through a foil into the gas, the accelerating electric field would tend to return the backscattered electrons toward the gas.

A foil normally separates the tube from the gas. Scattering in the foil adds some mean angle to the incident electrons according to the root of sum of the squares of the incident and scattered mean angles. Foil scatter tends to fill in the neck of deposition profile and foreshorten the range.

A cell wall located within an electron range of the point of injection distorts the deposition profile. Electrons impacting the wall are partially absorbed and partially backscattered. Since the fraction of the energy backscattered increases with the atomic number Z of the wall, a high Z wall will increase the relative energy deposited uniformly in the cavity. Depleted uranium backscatters 40% of the incident electrons at up to 70% of their incident voltage. In practice, however, the use of such a wall might contaminate the gas with impurities.

We now consider the superimposition of beamlets of electrons in various laser-cell geometries. First envision a 2-cm-wide beam of electrons incident on a standard 2 × 2-cm rectangular cell. For illustrative purposes, we use 1-MeV electrons, 0.005-cm-thick aluminum foil, and 10 atm of xenon contained in a stainless steel cell. We note that 18% of the energy is backscattered, 50% deposits in the walls, and only 20% deposits in the gas, with the remaining energy lost in the foil.

To increase the fraction of the energy deposited in the cell we inject the electrons toward the cell center, as shown in Fig. 11. However, the deposition profile across the cell is still nonuniform. By injecting the electrons from two sides, the transverse uniformity is increased as shown in Fig. 12.

A more natural geometry is cylindrical injection into the cell. With a cell diameter d having a value $d \sim 0.5\ R_0$, uniform deposition is provided with ~50% of the gun energy deposited in the cavity.

Later sections will describe gun configurations to pump the desired cell geometries.

ELECTRON GUNS

Of the many types of electron guns such as thermionic (52), glow (53), cold cathode (54), field emission (55), photo emission (56), multipaction (57), and plasma (58), only the first three have found widespread use for pumping lasers. The first two are typically used for low voltage (0.1-0.3 MV), low-current density ($\lesssim 10$ A/cm^2) and long pulse ($\gtrsim 1$ μs to continuous). The third covers this range and extends to high voltage, greater current density and shorter pulse widths but not continuous.

The former guns are limited to the long pulse width necessary to produce reasonable energy density in the gas at their intrinsically limited current density. The latter gun is limited to pulsed operation by plasmas in the gap. Additionally the former guns may be grid controlled where the latter may not, again because of plasma closure.

The operating regimes for the guns overlap and one may use post acceleration to obtain higher voltage or focusing to increase current density on the first two guns. However, we will distinguish the natural

regimes of operation as applied to pumping large volumes of gas, i.e., for beam areas $\sim 10^2$ to 10^6 cm^2.

Practical operating conditions, maintenance, and failure modes must also be considered in selecting or designing a gun. For example, heater or plasma production power requirements are important to consider in system economics. Inadvertent contamination of the cathode because of window failure can be important to the gun lifetime.

Thermionic Guns

Thermionic emission occurs from a heated conductor according to the Richardson-Dushman (59) relation

$$J = A T^2 e^{-\frac{eW}{KT}}, \tag{22}$$

where A is 60.2 A/(cm^2/deg^2) and W is the thermionic work function.

Figure 13 summarizes the saturated current density for several types of cathodes. Gallagher (60) has reviewed the relative effect of poisoning on these several cathodes as shown in Fig. 14.

The oxide cathode may be dismissed because of its easy susceptibility to oxygen poisoning. Pure tungsten cathodes are rugged, but since cathodes above about 1000°C are dominated by radiation loss, which varies at T^4, its use should be evaluated carefully. Cathodes such as lanthanum hexaboride, thoriated tungsten, and barium tungsten (dispenser) offer a balance between susceptibility to poisoning and excessive heater loss. The latter two cathodes are receiving most widespread use for lasers. Thoriated tungsten is usually prepared in the form of wires and barium tungsten in the form of sheets (solids). Since the thorium or barium is admixed throughout the tungsten volume, the cathodes can be reconditioned (to some extent) after contamination.

The extraction of uniform beams at low-current densities (≤ 1 A/cm^2) and reasonable anode-cathode (a-k) gaps requires the use of a grid close to the cathode such that the grid-cathode (g-k) gap is space-charge limited. Current density and pulse width are then determined by the (g-k) potential. The risetime of the pulse is limited by the (g-k) capacitance (which must be charged) and by the drive-circuit inductance.

The beam electron trajectories are typically controlled by electrostatic optics such as the Pierce configuration (61) or other appropriately graded structures.

The insertion of any structure in the diode will cause a change in the electron trajectories. The grid, when placed close to the cathode (hence requiring small control bias), acts as an electron lens. Amboss (49) has shown that such grid apertures focus the beam close to the grid and give rise to a displacement (w_g) at the anode relative to the axis of the aperture of

$$w_g = \frac{a}{2}\left[\frac{V_{a-k}}{V_{g-k}} - 1\right]^{1/2}, \tag{23}$$

where a is the aperture radius. Such deflection is important for narrow beams, and such beam divergence may cause electron loss in a foil support.

Glow Discharge Guns

Glow-discharge electron guns have been used for some time. These guns have taken the form of diodes with solid cathodes (62) or hollow cathodes (63) with grid control (64). However, such guns have only recently been applied to laser pumping (65).

Examples of the diode glow-discharge electron gun is shown in Figs. 15 and 16. A low pressure gas ~10-50 μ helium fills the gun. The voltage is dropped primarily across an ion sheath close to the cathode. The remainder of the gun is roughly at equipotential with the anode. Ions having up to the full-gun voltage impact the cathode surface releasing secondary electrons that are accelerated through the sheath. The ions are generated primarily by electron-atom collisions in the sheath region. Electrons are also generated in the sheath region (throughout the accelerating region) and consequently such guns are characterized by widespread electron energies for a fixed accelerating voltage.

The hollow-cathode glow-discharge gun has been developed by Bayless (64) for large-area beam production as illustrated in Fig. 17. The gun consists of an electron production region and a triode acceleration region. The entire diode is filled with 10-50 mtorr of helium. Within the hollow-cathode region, an ignitor electrode at a potential of $\lesssim$1 kV produces plasma. The low-voltage electrons within this region cause ionization. The ions increase the electron density through collisions with the large-area hollow-cathode wall. Ion acceleration occurs through a sheath as in the previously described gun, but only to potentials $\lesssim$1 keV as controlled by the ignitor electrode, thereby reducing sputtering. The electrons are extracted from the hollow-cathode container through a grid structure that is biased and that faces the triode assembly. This grid structure may be biased to provide current control. Normally electrons are extracted from the plasma sheath and controlled by the interelectrode grid with a bias ~100 V. They are then accelerated between this grid and the anode. In the acceleration region electron-ion collisions are negligible and hence little divergence is introduced by the gas in this region. The grid-anode spacing d_{ga} is selected in concert with the voltage so that neither vacuum or gas breakdown occurs. These breakdown limits are determined by the Cranberg vacuum breakdown criterion (66) and the Paschen gas-breakdown curve (67) as shown in Fig. 18.

Cold Cathode Diodes

Whereas the thermionic and glow electron guns are limited to low-current densities and hence long pulses to produce a specified electron energy deposition, cold cathode guns provide high-current densities and short pulses.

In its simplest form, the cold cathode is a smooth metal or graphite surface. More sophisticated forms use field enhancement provided by needles or blades, or metal-dielectric interfaces.

J. C. Martin (68) first utilized a variety of these cathodes for the production of reasonable area, high-current density electron beams.

Through extensive studies of such cathodes, Mesyats (69) discovered the mechanisms responsible for electron emission. Both Bradley et al. (70) and Parker (71) found that these emission mechanisms are relevant to the aforementioned cathodes.

Basic to the operation of these cathodes is the explosion of whisker microprotrusions on the cathode surface. As the applied voltage rises, field emission occurs from the microtips of the whiskers. The net field enhancement is a product (72) of a microscopic field-enhancement factor β_μ caused by local protrusions on the cathode surface and a macroscopic field-enhancement factor β_M caused by the gross cathode structure. The microscopic field-enhancement factor is a function primarily of the microprotrusion shape and not the size (73), and leads to field-enhancement factors (74) of $\beta_M \sim 10\text{-}100$.

The initial field emission at the microtip gives rise to heating and vaporation processes at the tip, which at local current densities $\sim 10^9$ A/cm^2 causes the explosive formation of a plasma (69). This plasma has a density $\sim 10^{17} - 10^{19}$ and expands rather symmetically from the microtip with a velocity $v_p \sim 2 \times 10^6$ cm/s relatively independent of the gap voltage or cathode material. The plasma from adjacent microtips blends together to form a smooth (69) plasma-cathode surface from which electrons are accelerated toward the anode.

Low-level voltage coupled from the pulse-forming line (prepulse) or an externally applied voltage may aid in the production of this plasma. Forester (75) and Mesyats (76) have shown that such preapplied voltages may lead to the production of a stable uniform-plasma surface. However, they show that certain conditions of preapplied voltages can lead to unstable operation. In such a case, most likely a few whiskers explode, drawing locally high currents leading to a local magnetohydrodynamic jetting (77) of the plasma across the gap. Although the precise mechanism is not clear, the unstable regime results in a nonuniform e-beam and gap closure at greater than 2 cm/us.

After an initial field emission and whisker explosion phase lasting a few nanoseconds, the space between the cathode plasma and the anode is space-charge limited (78). For a simple parallel-planar gap, the space-charge-limited impedance is given by

$$Z_{planar} = \frac{433}{V^{1/2}} \frac{(d_{ak} - v_p t)^2}{A} \ \Omega, \tag{24}$$

where the anode-cathode gap (d_{ak} in centimeters) has been corrected for the cathode plasma moving with velocity v_p in cm/μs with t in μs. V is the gap voltage in megavolts and A is the beam cross-sectional area in square centimeters.

Blade Cathodes. Blades are commonly used in cold-cathode electron guns at low-current density because macroscopic cathode-field enhancement is required at low-current densities ($\lesssim$50 A/cm^2) to form a cathode. The geometry for a single blade is shown in Fig. 19. The impedance for such a blade is given by

$$\bar{z}_{blade} = \frac{428}{V^{1/2}} \frac{p^2 (d_{ak} - v_p t)^2}{2\,\Delta w(\ell + \Delta w)} \quad \Omega, \tag{25}$$

where ℓ is the blade length in centimeters, Δw is the beam width at the anode plane in centimeters, and p^2 is a field enhancement factor. Typically the blade protrudes from a background plane, and Bradley and T. H. Martin (79) have empirically determined (at least for small gaps) the relation

$$\Delta w = 1.46\, h^{1/4} d, \tag{26}$$

where h is the blade height above the background plane. We (79) have also empirically determined a relation for the electron divergence from a single blade for the particular case where h = 0.25 cm as

$$\theta_d = 0.6\ t\ cm^{-1}(x/d) \quad x \lesssim \Delta w, \tag{27}$$

where x is the distance along the anode measured along the anode orthogonal to the blade.

While Singer (80) has described the use of single blades, Loda (81) and J. C. Martin (82) have employed multiple blades. Bradley et al. (79) have examined the gap impedance and beam divergence as the number of blades on a cathode support is increased. As shown in Fig. 20 the gap impedance varied smoothly as the number of blades increased between that for assumed independent blades and an assumed planar surface. Essentially the emitting surface increased from an array of plasma cylinders (corresponding to the plasma on each blade edge) to a flat-plasma surface as the plasma from the individual blades merged together. They also showed that the mean-beam divergence decreased as the number of blades increased, as expected from the consequent smoothing of the fields at the cathode surface.

Beam divergence is an important consideration in using blade cathodes (also thermionic wire cathodes) because of possible electron loss to a foil support as shown in Fig. 21. Such loss may be minimized by orienting the blades orthogonal to the foil support bars.

Solid Cold Cathode. At higher current densities ($\gtrsim$100 A/cm^2) graphite cathodes have been widely employed. A high-purity fine-particle graphite material is uniformly machined and cleaned. Such cathodes have provided reproducible beams for thousands of shots at $\sim$1 kA/cm^2 over periods of months even with occasional window failures (83).

The grading of cold cathode guns to provide Pierce-type electrostatic trajectory control is complicated by the fact that virtually all structures in fields sufficient to cause cold-cathode emission also emit. Jedynak (84) and Trump (85) introduced the use of dielectric coatings to suppress vacuum breakdown. J. C. Martin (86) used liquid (oil) coatings and Schlitt (87) used solid coatings to suppress undesired emission on cathode-grading structures.

Present investigations are attempting to find a durable coating for fields of 0.5-2 MV/cm.

Gun Geometry

As we move toward larger guns with higher total current, the effects of the beam self-magnetic field becomes important. Electron beam self pinch sets constraints on the maximum current and geometry. As an electron is accelerated toward the anode it is deflected by the self-magnetic field with gyroradius r_g. If this gyroradius is comparable to or less than the diode gap d_{ak}, the beam pinches and is cut off (43).

We consider a rectangular beam with a two-side injection and a cylindrically injected beam as shown in Fig. 22. The maximum deflection for an electron at the beam edge is given approximately by

$$\theta_{dr} = \sin^{-1}\left(\frac{I}{I_{AL}}\ \frac{2d_{ak}}{\ell}\ \pi\right) \qquad \text{(rectangular beam)}, \tag{28}$$

$$\theta_{dc} = \sin^{-1}\left(\frac{I}{I_{AL}}\ \ell n\ \frac{r_a}{r_c}\right) \qquad \text{(cylindrical beam)}, \tag{29}$$

where ℓ is the cathode length in centimeters, r_a is the cell radius in centimeters, r_c is the cathode radius in centimeters, and I_{ak} is 17 $\beta\gamma$ in kiloamperes.

Let us contrast two-sided rectangular and cylindrical injection for a particular set of parameters. Let I_{total} = 45 kA, V = 300 kV, d = 2 cm, cell width (diameter) = 2.5 cm, and ℓ = 20 cm. Also let the cells have the same active volume. Then

$$\theta_{dr} = \sin^{-1}\left[\frac{25}{34}\ \frac{2(2)}{20}\ \pi\right] = 25, \tag{30}$$

$$\theta_{dc} = \sin^{-1}\left[\frac{45}{34}\ \ell n\ \frac{1.25}{3.25}\right] = \sin^{-1}\ [1.26] \rightarrow \text{cutoff}. \tag{31}$$

The rectangular case is slightly pinched while the cylindrical case is cut off.

This case was selected to illustrate the drastic difference between the two geometries. The fundamental cause of the difference is the manner in which the anode current is returned to the diode, a factor neglected in previous diode models. As shown in the sketch, the current in the rectangular case is returned orthogonal to the optical axis and the current in the cylindrical case is returned parallel to the optical axis. The latter case gives stronger magnetic fields enhancing the tendency to cut off.

A way to utilize a cylindrical cell and avoid cutoff is to return the current along a radial ground plane from the anode (cell) as shown, thereby reducing the net magnetic-field intensity and approximate a "folded" rectangular geometry. This geometry also has the attribute that the electron trajectories are directed toward the center of the cell to provide uniform pumping.

The cylindrical cells reported by Ault (37) and Gerardo (88) are fed only from one side. They actually operate in a pseudocylindrical mode with currents configuring themselves to approximate the quasicylindrical scheme. That is, the return current flows nonsymmetrically on the cell (anode) opposite the cathode feed, thereby reducing the magnetic field on the feed side below cutoff. In a true cylindrical geometry, these diodes would be at or close to cutoff, pumping only the center of the cell.

Because of the diode self-pinch we are led to a modularization of the diode to *limit a module current and reduce the module self-pinch.* We will return to this question in a subsequent section.

Diode Grading

We have examined some cathode types and emission processes. We now consider the configuration of the diode to grade the electric field balancing the beam-space charge and self-magnetic fields so as to properly guide the electrons toward the laser cell. In general, we desire the electrons directed orthogonally toward the cell wall. In some cases we may want the electrons convergent toward the cell center to compensate for gas scatter in the cell, and in other cases we might settle for a divergent electron flow to facilitate construction of the diode.

We first review the case where the self-magnetic field is negligible, as it is in many low-current density ($J \lesssim 1$ A/cm^2) guns, then include the self-magnetic field effect for higher current-density situations.

Typically low-current density guns are grid controlled. Otherwise space-charge-limited operation would lead to excessively large (a-k) gaps and temperature-controlled emission would lead to nonuniform and non-reproducible beams.

The simple planar-diode divergence at the beam edge is caused by lens action in the grid and by nonuniformity in the space charge at the cathode edge. Thus a Pierce or other appropriate geometry is required to properly grade the net electric field in the diode. Amboss (49) has illustrated several geometries that control the electron flow while keeping the diode dimensions reasonable. Figure 23 shows two such geometries. Figure 23a uses a cylindrical sector cathode and planar anode and the electrons are directed orthogonal to the cell wall. Figure 23b employs a purely cylindrical sector geometry. Although this geometry leads to a divergent e-beam, it has the attribute that the cylindrical vacuum vessel is easy to fabricate. Amboss also has illustrated in Fig. 24 how the idealized Pierce geometries for selected flows may be implemented in practice by proper termination of the electrode structures such that the equipotentials in the region of the beam approximate those for the Pierce geometry.

For cases where the self-magnetic field is negligible, one may simulate the fields by analog techniques such as teledeltos paper (89) or electrolytic tanks (89) provided care is taken to account for the space charge near the cathode. Such simulations are reasonably accurate, because to first order the electrons follow the electric field lines. Where the self-magnetic field is important, however, a self-consistant code including magnetic field effects must be used to numerically simulate the electron flow.

Utilizing such a code developed by Hermannsfeldt (90), Schlitt (21) has shown that curvature of the cathode for rectangular beams with intense magnetic fields ($J \sim 1$ kA/cm^2 and $I_{tot} \sim 100$ kA) can to some degree compensate for the self-magnetic pinch as shown in Fig. 25. He has further shown that a proper combination of cathode and anode shaping ca. be used to largely compensate for self pinch and provide an electron beam directed orthogonal to the cell wall as shown in Fig. 26. The above simulations (with experimental correlation) relate to the narrow dimension of a rectangular e beam, which has a large long-to-narrow dimensional aspect ratio. Magnetic compensation is also required in the long dimension.

With the higher current e beams, the effect of the magnetic fields from the anode return and cathode feed must also be compensated. The anode return-current effect was mentioned in the previous section. The cathode feed-current effect is best illustrated by the semiubiquitous center-fed rectangular cathode commonly used in CO_2 guns, as shown in Fig. 5. Because the current is fed to the center of the cathode and flows along the cathode toward the ends, it produces a magnetic field midway along the cathode that opposes, and is usually more intense than, the beam self-magnetic field. This results in a divergence of the electrons at the midpoints away from the gun center as shown in Fig. 27. Consequently, because of the foil supports typically employed in such guns, the current density is reduced and the electron penetration into the gas foreshortened. For CO_2 lasers having a cavity bias field, the current density may be increased at these points by increasing cathode emission. However, direct gas pumping with diodes that are already fully space-charge limited such effects produce unacceptable nonuniformities in pumping and alternative cathode feeds are required.

Diode Modularization

As we move toward larger cavity size and higher total currents, some point is reached at which electrostatic grading of the diode becomes intractable and we are led to a modularization of the diode (and perhaps source and feeds) to reduce the self-magnetic field per module with magnetic isolation of the modules.

The simple economics of optics leads us to desire laser beam diameters $\gtrsim$20-30 cm. Because gas has a modest energy-storage density, we require long amplifier modules ($\ell \sim$ 1-10 m). Thus we envision long, thin cavities. Two attractive geometries for direct e-beam pumping are cylindrical and slab, as shown in Fig. 4. The cylindrical geometry is a natural match to the laser beam and utilizes radial electron injection. The slab geometry is designed for multiple-pass energy extraction and is pumped for two sides by the e beam.

The diode modularization choices are two-fold involving a host of small beams or involving rectangular beams. The application to the two geometries is quite similar except that in the cylindrical geometry the rectangular beams may be oriented parallel to the axis (bar geometry) or wrapped around the axis (hoop geometry) as shown in Fig. 28.

Electron Beam Drift

In early e-beam pumped gas-laser experiments, the e beam was drifted through neutral gas from the gun to the cell, providing for decoupling of

the laser from machine shock (91) and for control of the current density independent of the gun parameters (92). In such drift it is necessary to produce an e beam of minimum transverse energy by controlling gun emittance and divergence and using thin foils separating gun-drift chamber. The minimization of the e-beam transverse energy is important to drift efficiency (20), propagation through cell window supports (20), and e-beam focusability (93). The latter is mentioned because one may want to focus the e beam to penetrate small, differentially pumped apertures isolating the gun from the cell (93) or to control the current density (92).

SOURCE TECHNOLOGY

Overview

The e-beam pumped gas laser may be envisioned as one in which random electron energy from the wall plug is space-time compressed and improved in directional quality. The overall process is shown in the block diagram of Fig. 29. From the wall plug the electrical energy is transformed to high voltage and stored. A pulse-forming network then shapes the electrical pulse applied to the electron gun. The e beam from the gun is directed into the gas where the energy is stored in an appropriate population inversion. In the optical amplifier mode, the energy is extracted in a high-quality optical beam. Most promising visible-laser transitions currently identified must be pumped in times from 0.01 to 1 μs. Within this temporal regime, there are two ways to form pulses, using either distributed or lumped pulse-forming networks (PFN's). The former may be as simple as a section of charged cable and the latter may be the lumped equivalent of this cable. Which circuit may be used is determined by the rise time L/R time constant of the component inductances and the load resistance, and by the $\sqrt{LC}$ time constant of the circuit. Nominally the distributed circuit is required for very short or very powerful pulses.

Distributed circuits are pulse charged at high voltage and during charge act as a capacitor. Examples of the pulse charger are the Marx (94), LC generator (95), transformer (96), and Van de Graff (97). In the Marx and LC generator an array of capacitors is charged at low voltage and switched (erected) to high voltage. The transformer principle is well known, but great care must be taken to prevent high-voltage breakdown. The Van de Graff employs a belt to slowly charge the PFL. The latter two circuits have not been successfully used for more than a few kilojoules.

Alternate techniques exist to produce similar results such as charging distributed or lumped lines (98) at low voltage and erecting them to high voltage. The novel spiral generator (98) synthesizes both functions.

The lumped circuit approach was extensively developed during the 1940's for pulsed radar and has recently been extended to high-voltage application. The simplest circuit involves only a high-voltage capacitor (Marx) to approximate a square pulse as shown in Fig. 30. The rise time is determined by the system inductance and load resistance ($\tau_r \sim L/R$) and fall time by the capacitance and load resistance ($\tau_f \sim RC$).

In the next sections we will describe the source elements in more detail, and later mention switching and component breakdown.

Marx Generators

The Marx generator consists of a series interconnection of capacitors and switches. An example is given in Fig. 31, which shows a folded Marx and contains a pair of capacitors per switch. The capacitors are alternately (plus-minus) charged with respect to the central switch. Such a capacitor pair and switch constitute a stage. In this example, the first switch is triggered to erect the Marx. The key to precise erection is the use of interstage coupling, which in the example is provided by the capacitive coupling of the adjacent capacitor containers.

Considering the first two stages at the instant that the first gap is fired, we see a series circuit formed by the capacitors and switch capacitance and coupled back to the first capacitor by the intercontainer capacitance. Nominally the capacitors have values $C \sim 0.1\text{-}1$ μF, the switches $C_s \sim 10$ pF and the coupling $C_c \sim 1$ nF. Thus, in the two-stage loop, the loop voltage is distributed inversely with the capacitance and almost all appears across the unfired switch, thereby drastically overvolting and firing it. Thereafter the process repeats sequentially up the Marx. Because of the zigzag capacitor arrangement and because the switch overvoltage in this example is twice the stage voltage, this Marx is referred to as an S-type n = 2 Marx (99). The Marx, where only one switch is triggered, typically has an erection jitter of ~50 ns.

The erection jitter may be reduced if all switches are triggered. The jitter is minimized if alternate pairs of mid-plane switches are triggered separately as shown in Fig. 32. Since the alternate pairs of gaps are triggered, this is referred to as an m = 2 triggered Marx (94). These Marxs have jitter of ~2 ns. This low jitter is important to laser application for staging amplifiers or for synchronizing diagnostics.

The charge resistors were omitted from the preceding figures for clarity. A complete Marx is shown in Fig. 33, which is typical of those used in most new generation e-beam laser systems.

Alternatives of inductive charging, which is preferable for repetitively pulsed systems and resistive or inductive coupling, also exist. Clearly these elements must represent a high impedance to the erected Marx relative to the load. Fitch (94) has summarized the basic principles of operation for this and other Marxs, and gives a more detailed categorization of Marx types.

An important consideration in how quickly a Marx can deliver its energy or its suitability as a lumped-circuit element is the Marx inductance. This inductance arises from three main places, the capacitors, the switches, and the loop inductance between the Marx and the ground return (container). A rule of thumb for a well-designed Marx is that these three contributions be equal.

Resistive losses are also important to the efficient extraction of energy from the Marx. Generally such losses, aside from the easily evaluated charge and trigger losses, are distributed through the Marx, particularly within the capacitors (100) and also in the skin effect loss (101) of the elements.

LC Generator

The LC generator has been used to drive e-beam guns through distributed (95) or lumped (102) elements. Its principle of operation is shown in Fig. 34. The capacitors are plus-minus charged alternately. A *simultaneous* triggering of the switches causes alternate capacitors to ring through their contiguous inductors, reversing their polarity and placing the capacitors in series. This configuration excludes the switches from the erected circuit thereby reducing the net inductance by 1/3 of that for a Marx. However, a lack of synchronization or prefire of one switch causes most of the generator energy to flow through one switch. Because of this fault mode, LC generators are typically used for systems requiring only a very few switches.

Transformer

The transformer is suitable to supply high voltage for either lumped or distributed circuits. In either use it directly changes a high voltage capacitor from a low-voltage capacitor. The transformer is generally used in a double resonance mode (103) to achieve high-voltage gain and optimum energy-transfer efficiency. In this mode the primary and secondary resonant frequencies are selected equal ($\omega_0 = \sqrt{L_1C_1} = \sqrt{L_2C_2}$) and the coupling coefficient is selected to be $K = M/\sqrt{L_1L_2} = 0.6$.

Transformers supplying up to 5 MV have been used since at least 1928 (104). They have the advantage of apparent simplicity of design and ease of construction. However, in practice they have been limited to a few kilojoules or less, whereas the extensive Marx development has led to reliable systems for kilojoules to several megajoules.

Two basic transformer geometries have evolved. T. H. Martin (105) and Abramyan (96) have independently developed similar tesla designs as illustrated in Fig. 34. Others (106) have recently built 2-MV generators using this design. J. C. Martin (107) introduced the spiral wound transformer which has recently been applied by Rohwein (108) to drive high-current electron-beam guns as shown in Fig. 35. Abramyan (96) and J. C. Martin (109) have applied these two transformer types repetitively to pulsed systems.

Great care must be taken to properly grade the transformer for high voltage and to protect it from transients occurring during the secondary capacitor discharge into the load.

Distributed Pulse-Forming Lines

The basic pulse-forming line is shown in Fig. 36. The line is pulse charged from a Marx or transformer, and during slow charge acts as a capacitor as shown in Fig. 37. We will use Marxs in future discussions of the circuit elements. The line voltage, neglecting losses, is given by

$$V_L = V_M \frac{C_M}{C_L + C_M} (1 - \cos \omega t), \tag{52}$$

where

$$\omega = \sqrt{LC_N}$$

and

$$C_N = \left(\frac{1}{C_M} + \frac{1}{C_L}\right)^{-1}.$$

A voltage gain of up to two may be realized by decreasing the line capacity relative to the Marx capacity. Typically at or near the peak of the line-charging waveform, the switch is closed connecting the line to the load. The line discharge time Δt must be small compared with the Marx-line charge time to minimize energy loss back to the Marx.

The most common geometries for PFL's are coaxial (110) and flat plate (111), as shown in Fig. 38, although parallel bar (112) and disc lines (113) also find application. The characteristic impedances for the first two lines are determined by

$$Z_0 = \sqrt{L_\ell / C_\ell}, \tag{33}$$

where L_ℓ and C_ℓ are the inductance and capacitance per unit length. In practical dimensions, these are

$$Z_{oc} = \frac{60}{\sqrt{\epsilon_r}} \ln r_2/r_1 \qquad \text{(coaxial)}, \tag{34}$$

$$Z_{op} = \frac{377}{\sqrt{\epsilon_s}} \frac{a}{b} \qquad \text{(planar)}, \tag{35}$$

where ϵ_r is the relative dielectric constant of line dielectric; r_2, r_1 are the outer and the inner line radius respectively; and a, b are the plate separation and the width respectively.

The most common dielectrics are oil and water, which have time-dependent breakdown strengths according to (114)

$$E\, t_{eff}^{1/3}\, A^{1/10} = K, \tag{36}$$

where E is the electric field in MV/cm, t is the effective charge time in microseconds (defined as that time for which the voltage exceeds 63% of its self-breakdown value). A is the line electrode area in centimeters squared; K is a constant whose value depends on the liquid dielectric ($K = 0.5$ for oil and $K_+ = 0.5$ for water). Water breakdown is polarity dependent and K_+ corresponds to a positive field-enhanced electrode. The strength of a negative field-enhanced electrode for water is $K_- = 0.6$. Because of this polarity effect in water, the center electrode of a coax is usually selected to be negative if possible, thereby permitting optimum energy storage. If we select the criteria that breakdown from either electrode in a water coax be equally probable, then the natural characteristic impedance for a water line is 5.8 Ω. Similarly including an area effect for an oil line it is ~20 Ω. Usually one cannot deviate from these natural impedances by more than a factor of 2-3 without encountering breakdown problems or excessively large devices.

Solid dielectrics have been used in some lines, but problems of lifetime, edge grading, and absolute failure in the event of arcing has limited their practical use to $\lesssim$300 kV.

The electrical pulse length of a line, as determined by the velocity of the propagation of electromagnetic radiation through the volume is given by

$$\Delta t = \frac{2\sqrt{\epsilon_r}\,\ell}{C} , \tag{37}$$

where ℓ is the line length in centimeters, and C is the velocity of light in free space in centimeters per second. Combining the above relations, we obtain a useful relation

$$Z_o = \frac{\Delta t}{2C_L} . \tag{38}$$

When the switch closes connecting the line to the load, the resulting output pulse is determined by the relative characteristic line and load impedances as shown in Fig. 39. Thus, the line may be mismatched to achieve voltage or current gain, but at the expense of efficiency and the production of post pulses. The latter can usually be crowbarred from the gun. Throughout the range of interest to lasers, $0.2 \lesssim V \lesssim 5$ MV, either oil or water lines may be constructed. However, for certain applications mismatch is desirable since the natural line impedance is limited. For efficient x-ray production, the load is usually mismatched high and for high-current plasma experiments it can be mismatched low. Alternately series and(or) parallel combinations of lines can be used to extend the range of operation, but not without severe constraints imposed by cumulative losses and interface problems.

It is often convenient to use a Thevinen equivalent circuit (115) to describe the line discharge into the load during the main pulse as shown in Fig. 40, where V_C is the line-charge voltage. A standard textbook example is to show that maximum energy is transferred to the load when the impedances are matched. The circuit in this configuration is merely a voltage divider and load voltages are quickly determined. The load voltage for the matched case is half the charge voltage.

In reality switch and gun inductances must be included in the circuit as shown in Fig. 41. These inductances cause an e-fold rise time (and fall time) of

$$\tau_r = \frac{L_s + L_g}{Z_o + Z_L} . \tag{39}$$

This time must clearly be small relative to the pulse width to approximate a square wave. Minimum rise time is important to lasers because low-energy electrons deposit primarily in the foil and adjacent gas causing excessive foil heating and nonuniform pumping. Too small of a switch inductance relative to the gun inductance can be detrimental because when the switch is first closed the inductive divider circuit applies most of the voltage across the gun, is up to twice the matched (or normal) gun voltage, and might cause the gun insulator to flashover.

The necessity to charge the PFL to twice the desired gun voltage led Blumlein (116) to develop a circuit (now named after him) that is charged to only the gun voltage as shown in Fig. 42. This circuit is matched if $Z_{01} + Z_{02} = Z_L$. The high-voltage flat-plate Blumlein was developed by J. C. Martin and the coaxial Blumlein by D. Martin. In practice a folded Blumlein is commonly used as shown in Fig. 43. This configuration saves space and permits the common floating electrode to be supported between the other two electrodes. In the coaxial folded Blumlein if the breakdown probability on all electrodes is roughly equal, then the characteristic impedances of the lines differ. It should be noted that the unbalanced Blumlein applies a prepulse across the gun during charge. Consideration must be given as to the effect of the prepulse on the gun, particularly the cold cathode gun.

There are several circuits for PFL's that improve the rise time applied to the load. The only one we will describe uses series-peaking gaps in series with the PFL. Such gaps are usually used with a transfer line interconnecting PFL and gun. The gaps may be located along the line or at the gun. In addition to reducing the voltage rise time at the gun, these gaps provide decoupling of the gun from the PFL during charge.

A further reduction in prepulse may be obtained by using shunt resistors across the gun, provided their resistance is several times higher than the characteristic line (or load) impedance. Shunt resistors give added flexibility in source applications because they can be varied in value, as gun current is varied, such that the PFL remains matched. Thus, the waveform can remain unchanged even though the gun is run at very low currents.

Pulse Forming Networks

The simplest, and thus far most widely used circuit for driving laser guns at longer pulses involves simply a Marx connected to the gun as shown in Fig. 44a. The gun voltage is given by

$$V_L = \frac{V_m}{\sqrt{R^2 - 4L/C}} \left(e^{-t/RC} - e^{-tR/L}\right). \qquad (40)$$

The waveform applied to the load is shown in Fig. 44b, where the rise time is determined by L/R and the fall time by RC. Since the electrons pass through a foil into the gas, those below a certain threshold are stopped in the foil resulting in a more rectangular pump pulse as shown in Fig. 45. The consequent foil heating may lead to foil failure. Milde (117) and Ault (37) have developed such systems providing ~100 J at a few hertz.

By increasing the capacitance and using a crowbar, one can also approximate a rectangular pulse. Such systems have been made by Kolb (118) and Loda (119). The crowbar reduces foil heating but at a significant sacrifice in energy. Tradeoffs can be made concerning the amount of permissible droop and wasted energy. For systems smaller than a few kilojoules, this approach is sometimes economically attractive, although for high frequency systems the dissipation of wasted energy can be a problem.

then $R_L^2 = L/C$ or $\tau/R_L = R_L C$. A symmetrical rise and fall are provided and a characteristic frequency of $\omega = 1/\sqrt{LC}$ is obtained.

Tuned resonant-circuit elements can be added to provide a more rectangular waveform, in essence adding higher Fourier components to the waveform. This approach was developed by Guilleman (120) and was summarized by Glasoe and Lebacqz (121).

A trapezoidal current waveform as shown in Fig. 45 may be represented by a Fourier series

$$i(t) = I \sum_{\nu=1}^{\infty} b_\nu \sin \frac{\nu\pi t}{\tau} , \tag{41}$$

where $b_\nu = \frac{4}{\nu\pi} \frac{\sin \nu\pi a}{\nu\pi a}$ for $\nu = 1, 3, 5, \ldots$ A ladder network can be constructed to produce this waveform as shown in Fig. 46 where

$$i_\nu = V_o \sqrt{\frac{C_\nu}{L_\nu}} \sin \frac{t}{\sqrt{L_\nu C_\nu}} , \tag{42}$$

and

$$L_\nu = \frac{Z_o \tau}{\nu\pi b_\nu} ,$$

$$C_\nu = \frac{\tau}{Z_o} \frac{b_\nu}{\nu\pi} .$$

This basic circuit can be transformed into alternate forms by using Fosters Reactance Theorem (122) (partial fraction expansion) or Cauers Reactance Theorem (122) (continued division). The approach is to write the impedance for the basic circuit and apply one of the foregoing theorems to develop an alternate physically realizable circuit. Examples of circuits thus derived are shown in Fig. 47. These circuits are referred to as Gulliman type A, B, or C circuits.

The degree of approximation to a trapezoidal wave is determined by the number of sections used in the network, as illustrated in Fig. 48 showing normalized waveforms for 2, 3, and 5 section networks.

A ladder network similar to type B but having all inductors and capacitors of the same value has been used widely. It has the advantage that all components are identical, thereby facilitating construction.

Riepe (102) has developed a compersating circuit, shown in Fig. 49, that improves the current rise time at the load.

These circuits have been widely applied to pumping CO_2 as illustrated in the paper by Riepe (102). The type A circuit has been employed in the

megavolt range up to 100-kJ total energy. Ury (123) used a water capacitor in conjunction with a Marx and Smith (124) developed a solid-capacitor tuned-element network.

Other Topics

Switching, insulator breakdown, and flashover form an interesting subject but are too extensive for inclusion in this lecture. Much of the basic information is contained in the paper by J. C. Martin (114). More detail on particular subjects can be gleaned from the various publications such as those by Denholm (125) or Früngel (126).

EXAMPLES OF TECHNOLOGY

Since the e-beam pumped visible-gas laser is so new, entire systems have not yet evolved. We, therefore, give examples from LLL of complementary sources illustrative of those devices on which research concerning these systems has been and is being, done. We then give hypothetical examples of how one might utilize this technology for high peak power or high average-power amplifiers. Most of the systems concepts required such as uniformity, mode control, interstage isolation, etc. are illustrated by the complete CO_2 system developed by Manes (127).

MEG (Megavolt Electron Generator)

MEG I was developed interactively by LLL and Maxwell (110). It provides a 2 × 10 cm e beam at 1 MV, 100 kA, and 50 ns to transversely pump a laser cell as shown in Fig. 50 and Fig. 51. Pump energy densities range to 5 J/cm^3.

The Marx generator is composed of 28 stages. Each stage, having two 1.4 μF capacitors and a mid-plane triggered electrode is mounted on a tray. All switches are triggered in the m = 2 mode.

The water dielectric PFL is 45 cm in diameter. An overvolted SF_6 switch connects the PFL to a transfer line.

The diode has a flat plexiglas insulator and uses a graphite cold cathode.

System jitter from command trigger to e-beam output is ~2 ns and reproducibility is ~95%.

During charge of the line, the equivalent circuit shown in Fig. 52 applies. Internal Marx losses, primarily associated with the capacitors, produce a ringing voltage gain of 80% from the Marx to the PFL. The capacitances of these elements is equal to minimal residual-line energy and hence afterpulse.

During discharge of the line, the equivalent circuit of Fig. 52 applies. The output current waveform was predicted from this circuit and is compared against the measured waveform in Fig. 53. Numerical analysis of such circuits permits the designer to vary the length and size of the various system elements to manipulate the waveform and produce virtually any desired waveform.

A second source, MEG II, was developed, again interactively by LLL and Maxwell, to provide a wider transverse e beam of 2 × 50 cm as shown in Fig. 54. This machine uses peaking gaps midway along the transfer line to reduce the e-beam rise-time as shown schematically in Fig. 55. A typical current waveform is shown in Fig. 56. A novel semiconical oil line is used to flare out from the 45-cm diameter PFL to the wider diode dimension. The PFL switch in this machine is of an advanced design as sketched in Fig. 57. This switch can be run at higher pressure and hence lower inductance than the switch on MEG I.

These MEG sources are dedicated to laser experiments. Electron beam and diode development is conducted on a separate source (a PI 422) and is being modified by Schlitt to provide 25 kJ at 2 MV in 50 ns. This source is conceptually similar to MEG I except that a coaxial transformer is used to interconnect the PFL and diode.

Kinetics Source: LAMP (Laser Atomic and Molecular Physics)

The larger sources are ideally suited for laser experiments, particularly those relating to energy extraction. A need has developed for a small source tailored for kinetics studies at a high data rate.

We have selected a commercial linac injector (128) gun for this application. This grid-controlled gun, shown in Fig. 58, has a barium-oxide impregnated tungsten-matrix cathode with an emission area of 20 cm^2. The grid voltage is supplied by a 50-Ω coaxial feedthrough. The pulse rise time is limited to 1.5 ns by the 50-pF grid to cathode capacitance.

The gun operates at 100 kV. The Pierce optics focus the 40 a e-beam to 2.5-cm diameter at the gun face as shown in Fig. 59. At this face a 0.01 × 2-cm e beam is passed through a 2-μ-thick T_i foil into a gas cell.

In this configuration, the gun can-pump xenon, for example, to ∿1 J/cm^3 at 100 Hz. Cooling is provided by conduction to the walls. The grid control permits pulses from a few ns to a few μs at constant energy density in the gas.

Hypothetical KrO Power Amplifier

Because the field of e-beam pumped visible lasers is so new, with interesting candidates arising only during the past year, no systems exist to illustrate application of the technology. The state of the art is characterized by a quest for new laser media and an assessment of the applicability of known media. As a part of this assessment we have developed hypothetical models based on, in some cases, very preliminary data concerning the detailed pump physics and system kinetics. The two examples presented are selected from such studies. They are presented as "problems for the student" because they are incomplete and involve a host of options and tradeoffs which may be considered.

The KrO system was first developed by Murray and Powell (31) on MEG I using an in situ process. They and also Hughs et al. (32) have subsequently examined a photolytic transfer pump system wherein Ar_2^* radiation from an e-beam pumped cell was transferred to a separate cell containing N_2O. Laser action was observed for the in situ process and gain measured for the photolytic transfer. Recently, Turner and Taska (28) have demonstrated ∿30% efficiency for Ar_2^* fluorescence using a 1-μs e-beam source.

The impact of this result on the $O(^1S)$ system is being evaluated. More detailed analysis of the $O(^1S)$ laser is under active study at several laboratories. These studies include comparisons of in situ and photolytic transfer pump schemes, optional pump techniques including e-beam-TEA and discharge, and energy extraction experiments in a power-amplifier configuration.

For purposes of this model, we use the data of Murray and Powell determined on MEG I. We reiterate that application of these data to a 250-J power amplifier is a vast extrapolation from the existing experiment, but the extrapolation has been made to permit an assessment of the related e beam and source technology. Such modeling is necessary to evaluate the feasibility and economics of possible use of the $O(^1S)$ laser to fusion.

Using MEG I, Powell and Murray (129) have determined the following parameters for KrO:

$$\sigma = 1 \times 10^{-20} \text{ P cm}^2, \tag{43}$$

$$\varepsilon_{sat} = 35/\text{P J/cm}^2, \tag{44}$$

$$\varepsilon_{v\ell} = 5 \times 10^{-3} \text{ J/cm}^3, \tag{45}$$

$$\eta_\ell = 0.4\%, \tag{46}$$

where P is the rare gas pressure in atmospheres.

We consider a 250-J power amplifier with a stage gain of 5 and assume that energy can be uniformly extracted by using apodized apertures. A 10-cm-diam. cylindrical-laser cell would have an output optical flux of 3.5 J/cm^2, near the state of the art for optical components.

Selecting an operating pressure of 20 atm, the saturation flux is 1.75 J/cm^2. The gain is determined by

$$g = \frac{\varepsilon_{v\ell}}{\varepsilon_{sat}} = 0.29\%/\text{cm}. \tag{47}$$

The amplifier length to achieve these conditions is given by (130)

$$L = \frac{1}{2g} \ln \frac{e^{2\,\varepsilon_o/\varepsilon_{sat}-1}}{e^{2\,\varepsilon_o/(G\varepsilon_{sat})}-1}, \tag{48}$$

$$= 650 \text{ cm},$$

where ε_o is the amplifier output flux and G is the stage gain. Since the input pulse is below saturation, the optical extraction efficiency is (130)

$$\eta = \frac{\varepsilon_o}{\varepsilon_s} \frac{(1 - 1/G)}{g_o L} = 0.85. \tag{49}$$

The source parameters are determined from the relations in the test. Using Eq. (18)

$$\zeta = 2.5 10^{-4} \text{ Mp} = 0.42, \tag{50}$$

then

$$V = \mathcal{E}r = 2.1 \text{ MV}, \tag{51}$$

which is the voltage necessary to uniformly pump a 10-cm-diam. cell at 20-atm pressure. The current density pulsewidth product necessary to obtain the desired electron-energy density for $\eta_{e\ell} = 1\%$ is

$$J\Delta t = \frac{\epsilon_{ve}}{\zeta} = 1.2. \tag{52}$$

The pump time is limited by the $0(^1S)$ lifetime, which in the MEG I experiments was $\sim$0.7 μs. Thus, we select a pump time of 50 ns. The current, therefore, is 24 A/cm^2.

The total gun energy is $\sim$60 kJ with efficiencies of $\sim$50% of electron energy deposited in the cell, 1% pump efficiency, and $\sim$85% extraction efficiency. The stored energy in the stage would be extracted from this stage by a subnanosecond optical pulse generated in previous stages.

For pumping this geometry a modularized diode of the hoop geometry is required. With an anode-cathode gap of 20 cm, a module length of between 40 and 70 cm can be graded to deliver the electrons orthogonally to the cell. We select 10 modules of 65 cm each that are contiguously connected along the cell.

The total source current of 500 kA requires a 4.2-Ω/pulse-forming line. Even 10 separate PFN's each connected to a diode would be too inductive to produce a 50-ns pulse. We therefore are compelled to select a distributed PFL using water for compactness. By employing two parallel coaxial 8.4-Ω PFL's, the energy is better distributed to the laser cell.

Five diode segments are grouped and connected to each line. The 100-kJ, 4.4-MV Marx required is well within the state of the art. A final amplifier might appear as shown in Fig. 60.

On the whole, the pulse-power technology for this illustration and even larger amplifiers is within the state of the art. The E-beam diode configuration is rather new and specific problems such as current feed to the cathodes and its magnetic field influence on trajectories and diode grading are presently being parametrically studied.

Hypothetical He_2^+-N_2^+ High Average-Power Amplifier

This laser system is far from being fully characterized. Since it is such a high gain system and has such short storage time, it is not attractive for a high peak-power system. However, it might be attractive for a high average-power system (defined here as $\sim$1 kW at $\sim$1 kHz). Thus, we make certain assumptions concerning the rather limited kinetic data and develop a hypothetical source to pump the laser at modest efficiencies.

We assume, based on the Collins data (29), that an efficiency from electrons to laser (η_ℓ) of 2% is reasonable. Concerning the source, we expect that with proper charging etc., a plug to electron deposition efficiency of 30% can be achieved in a well designed source cell.

We further assume that the energy is uniformly extracted from the amplifier by a saturating flux from an oscillator. Such an oscillator might employ an unstable resonator to produce a low mode signal (131).

Since helium is a low Z gas, we desire a low voltage gun. The lowest reasonable voltage for which electrons can penetrate the foil is 200 kV. Recalling that $\xi = 2.510^{-5}$ Mp, we obtain a cell width (according to Eq. (18)) of $w = V/\xi = 5$ cm.

The pump pulse width may be estimated from the experimental lifetime, with the upper-state lifetime placing a probable longer bound on the pulse-width. The upper-state fluorescent lifetime for N_2^+ ($B^2\Sigma_\mu^+$) is (29) 66 ns.

Assume that we desire a pump-energy density $E_{V\ell}$ of 0.02 J/cm^3 and selected $\xi \simeq 0.014$ J/cm^3 from Collins since its parametric variation is unknown. Since $J\Delta t = E_{V\ell}/\xi$, we obtain $J = 10$ A/cm^2 for a 50-ns pump pulse. The anode-cathode gap is therefore $\sim d = 4$ cm.

Somewhat arbitrarily, we assume a 5 × 5 × 100 amplifier. At 0.02 J/cm^3 the pump energy required is 50 J. Roughly half the e-beam energy might be deposited in the cavity by using the centrally directed e beam as described earlier. Thus, the source must be ~160 J.

At 1 kHz, such an amplifier might provide ~900 W at 0.6% net efficiency. We now ask what might preclude rep-rate operation. Of particular concern are parasitic losses, foil survival, and source constraints, i.e., switching.

Parasitic losses are probably not a problem according to a study of high-gain amplifiers (131) since the bias fluence saturates the transition.

We have concerned ourselves with window-heating problems. Calculations (50) of foil temperatures using a quasi-steady-state approximation shows that the foil may be adequately cooled by radiative and helium convective losses. We notr that the average current loading is ~1 mA/cm^2, a value comparable to the upper operating regime for the foil operation of cw CO_2 lasers containing large fractions of helium (the helium is important for cooling). There is no question that foil lifetime will be one of the most critical engineering tasks in developing high average-power direct e-beam pumped laser systems. These initial calculations show that control of foil temperature appears tractable.

Recent advances in high-voltage rep-rated switch technology indicate that the switching problem is tractable using gas or vacuum switches. However, some further engineering and optimization will be required.

ACKNOWLEDGMENT

Many aspects of the material presented reflect the significant contributions of my co-workers: J. C. Clark, E. V. George, P. W. Hoff, W. F. Krupke, J. R. Murray, H. T. Powell, C. K. Rhodes, L. G. Schlitt, J. Taska, and C. E. Turner.

We assume, based on the Collins data [29], that an efficiency from electrons to laser (η_E) of 2% is reasonable. Concerning the source, we expect that with proper charging etc., a plug to electron deposition efficiency of 30% can be achieved in a well designed source cell.

We further assume that the energy is uniformly extracted from the amplifier by a saturating flux from an oscillator. Such an oscillator might employ an unstable resonator to produce a low mode signal [131].

Since helium is a low Z gas, we desire a low voltage gun. The lowest reasonable voltage for which electrons can penetrate the foil is 200 kV. Recalling that $\xi = 2.5 \times 10^{-4}$ Mp, we obtain a cell width (according to Eq. (18)) of $w = V/\xi = 5$ cm.

The pump pulse width may be estimated from the experimental lifetime, with the upper-state lifetime placing a probable longer bound on the pulse-width. The upper-state fluorescent lifetime for $N_2^+(B^2\Sigma_u^+)$ is [29] 66 ns.

Assume that we desire a pump-energy density E_{VI} of 0.02 J/cm^3 and selected = 0.014 J/cm^3 from Collins since its parametric variation is unknown. Since $Jdt = E_{VI}/\xi$, we obtain $J = 10$ A/cm^2 for a 50-ns pump pulse. The anode-cathode gap is therefore d = 4 cm.

Somewhat arbitrarily, we assume a 5 × 5 × 100 amplifier. At 0.02 J/cm^3 the pump energy required is 50 J. Roughly half the e-beam energy might be deposited in the cavity by using the centrally directed e beam as described earlier. Thus, the source must be 100 J.

At 1 kHz, such an amplifier might provide 900 W at 1% net efficiency. We now ask what might preclude rep-rate operation. Of particular concern are parasitic losses, foil survival, and source constraints, i.e., switching.

Parasitic losses are probably not a problem according to a study of high-gain amplifiers [131] since the bias fluence saturates the transition.

We have concerned ourselves with window-heating problems. Calculations [50] of foil temperatures using a quasi-steady-state approximation shows that the foil may be adequately cooled by radiative and helium convective losses. We note that the average current loading is 1 mA/cm^2, a value comparable to the upper operating regime for the foil operation of cw CO_2 lasers containing large fractions of helium (the helium is important for cooling). There is no question that foil lifetime will be one of the most critical engineering tasks in developing high average-power direct e-beam pumped laser systems. These initial calculations show that control of foil temperature appears tractable.

Recent advances in high-voltage rep-rated switch technology indicate that the switching problem is tractable using gas or vacuum switches. However, some further engineering and optimization will be required.

ACKNOWLEDGMENT

Many aspects of the material presented reflect the significant contributions of my co-workers: J. C. Clark, E. V. George, P. W. Hoff, W. F. Krupke, J. R. Murray, H. T. Powell, C. K. Rhodes, L. G. Schlitt, J. Taska, and C. E. Turner.

1. J. Nuckolls, J. Emmett, and L. Wood, Phys. Today (August, 1973).

2. J. Nuckolls, Lawrence Livermore Laboratory, Rept. UCRL-74345 Rev. 1 (1973).

3. A. Penzkofer and W. Kaiser, Appl. Phys. Lett. 21, 427 (1972).

4. E. B. Snavely, Lawrence Livermore Laboratory, Rept. UCRL-75725 (June 11, 1974).

5. E. B. Snavely, in Proc. Conf. on Lasers and Engineering Applications (May 28-30, 1975).

6. C. K. Rhodes, IEEE J. Quantum Electron. 10, 153 (1974).

7. J. R. Murray, in Proc. Physics of Quantum Electronics (Crystal Mountain, Washington, July, 1973).

8. C. F. Judd, Notes This Meeting.

9. R. T. Powell et al., Digest of Technical Papers, CLEA (May 28-30, 1975), p. 27.

10. C. B. Collins and A. J. Cunningham, Univ. Texas at Dallas, Rept. UTDP-ML-03 (March 1975).

11. J. W. Chamberlain, Physics of the Aurora and Airglow (Academic Press, 1961) and International Auroral Atlas (Edinburgh University Press, 1963).

12. H. Kishbeth and O. K. Garriott, Introduction to Ionospheric Physics, (Academic Press, 1969).

13. H. S. W. Massey and R. L. F. Boyd, The Upper Atmosphere, (Hutchinson, 1958).

14. Unpublished.

15. R. T. Powell et al., Digest of Technical Papers, VIII, Int. Quantum Electron. Conf., postdeadline paper, June 10-13, 1974.

16. C. B. Collins et al., Digest of Tech. Papers VIII IQEC 62 (1974).

17. B. Bernstein and I. Smith, IEEE Trans. Nucl. Sci. 20, 294 (1973).

18. I. Smith, in Proc. 15th Symp. Electron, Ion, and Laser Beam Tech. (Colorado Springs, Colorado, May 21-23, 1975), to be published.

19. H. H. Fleischmann, Phys. Today 55 (May 1975); J. Benford, Laser Focus, 45 (July 1975); A. Kolb, IEEE Trans. Nucl. Sci. 22, 659 (1975); and G. Yonas, Sandia Laboratories, Rept. SAND-74-5367 (1974).

20. L. P. Bradley, Lawrence Livermore Laboratory, Laser Fusion Program Report, (July-Dec. 1973), p. 146.

21. L. G. Schlitt et al., Bull. Am. Phys. Soc. 19, 1292 (1973).

22. T. F. Stratton et al., IEEE J. Quantum Electron. 157 (1975).

23. R. W. Dreyfus and R. T. Hodgson, IBM, Research and Development Rept. RC 3618 (1971).

24. A. W. Ali et al., Appl. Opt. 6, 2115 (1967).

25. T. J. Davies and M. A. Nelson, Appl. Opt. 12, 880 (1973).

26. D. A. McArthur and J. W. Poukey, Phys. Rev. Lett. 32, 21 (1974).

27. Yu. V. Tkach et al., Sov. Phys. JETP 35, 886 (1972).

28. C. E. Turner et al., in Proc. of Gaseous Electronics Conference, (Rolla, Missouri, Oct. 21-24, 1975), to be published.

29. C. B. Collins and A. J. Cunningham, Appl. Phys. Lett. 27, 127 (1975).

30. G. Black, Stanford Research Institute, Rept. MP 7504 (Jan. 15, 1975), and private communication.

31. H. T. Powell et al., Appl. Phys. Lett. 25, 730 (1974).

32. W. M. Hughs et al., in Proc. Conf. on Laser and Engineering Applications, postdeadline paper, (May 28-30, 1975).

33. S. K. Searles and G. A. Hart, Appl. Phys. Lett. 25, 79 (1974).

34. R. Hunter, private communication.

35. N. G. Basov et al., Sov. Phys. JETP L 20, 53 (1974).

36. E. R. Ault et al., J. Quant. Elect. 10, 624 (1974).

37. E. R. Ault, Appl. Phys. Lett. 26, 619 (1975).

38. R. A. Gerber et al., Appl. Phys. Lett. 25, 281 (1974).

39. Yu. A. Akimov et al., Sov. J. Q. Elect. 1, 646 (1972).

40. Y. Aoyagi et al., Appl. Phys. Lett. 26, 24 (1975).

41. O. V. Bogdankevich et al., Sov. J. Q. Elect. 1, 184 (1971).

42. P. W. Smith et al., Appl. Phys. Lett. 25, 144 (Aug. 1974).

43. L. G. Schlitt and L. P. Bradley, The Scaling of Electron Beam Sources for Laser Fusion Applications, to be published as Lawrence Livermore Laboratory Report, 1975.

44. B. W. Schumacher, in Proc. 1961 Trans. 8th Vacuum Symp. (Pergamon Press, 1962).

45. R. B. Buksht et al., Sov. J. Quant. Elect. 2, 272 (1972).

46. R. D. Evans, The Atomic Nucleus, (McGraw-Hill, 1955,.

47. M. J. Berger and S. M. Seltzer, Tables of Energy Lasers and Ranges of Electrons and Positrons, (National Bureau of Standards publication).

48. *SANDYL — Sandia Livermore Laboratory, Rept. SCL-DR-720109 (1973).*

49. K. Amboss, in Proc. 6th Int. Conf. on Electron and Ion Beams (San Francisco, Ca., May 1974).

50. W. Lai, Lawrence Livermore Laboratory Engineering Note ENE 75-8 (1975), unpublished.

51. P. G. Kriukov and V. S. Letokhov, Techniques of High Power Pulse Amplification, Laser Handbook, edited by F. T. Arecchi and E. O. Schulz-Dubois (North Holland, Amsterdam, 1972).

52. J. H. Fink and B. W. Schumacher, Optik 39, 545 (1974).

53. J. H. Holliday and G. G. Isaacs, J. Vac. Sci. Technol. 38, 15 (1971).

54. R. K. Parker, J. Appl. Phys. 45, 2463 (1974).

55. W. P. Dyke, Sci. Am. 108 (1964).

56. A. Passner, Rev. Sci. Instrum. 43, 1640 (1972).

57. D. J. Liska, Proc. IEEE, 1253 (Aug. 1971).

58. D. V. Tremashvili et al., Zh. Eksp. Teor. Fiz. Pis'ma Red. 17, 11 (1973).

59. K. R. Spangenburg, Vacuum Tubes, (McGraw-Hill, 1948).

60. H. Gallagher, J. Appl. Phys. 40, 44 (1969).

61. J. R. Pierce, Theory and Design of Electron Beams, (Van Nostrand, 1954).

62. B. B. O'Brien, Jr., Appl. Phys. Lett. 22, 503 (1973).

63. M. A. Cocca and L. H. Stauffer, in Proc. 5th Electron Beam Symp., Boston, 1963 (Boston, Mass., March 28-29, 1963), p. 342.

64. J. R. Bayless, Hughs Research Laborato, Rept. N00014-72-C-0496 (1974).

65. R. K. Garnsworthy et al., Appl. Phys. Lett. 19, 506 (1971).

66. L. Cranbery, J. Appl. Phys. 23, 518 (1952).

67. S. C. Brown, Introduction to Electron Discharges in Gases, (Wiley, 1966).

68. J. C. Martin, private communication.

69. G. A. Mesyats et al., in 4th Int. Symp. on Discharges and Electron Insulation in Vacuum (Sept. 1-4, 1970), p. 82.

70. L. P. Bradley et al., 5th Symp. on Discharges and Electron Insulation in Vacuum (Poznan, Aug.-Sept. 1972), p. 159.

71. R. K. Parker et al., J. Appl. Phys. 45, 2463 (1974

72. D. H. Alpert et al., in Proc. 1st Insulation of High Voltage in Vacuum (Oct. 10-21, 1964), p. 1.

73. F. M. Charbonnier, in Proc. 1st Insulation of High Voltage in Vacuum (Oct. 10-21, 1964), p. 1 of appendix.

74. T. Utsumi et al., in Proc. 2nd Int. Symp. on Insulation of High Voltage in Vacuum (Sept. 7-8, 1966).

75. D. W. Forrester, in Proc. 15th Symp. Electron, Ion, and Laser Beam Tech. (Colorado Springs, Colorado, May 21-23, 1975).

76. S. P. Bugaev, E. A. Litvinov, G. A. Mesyats, and D. I. Proskurovskii, Usp. Fiz. Nauk. 115 (1) 101-20 (Jan. 1975).

77. J. C. Martin, private communication.

78. I. Langmuir and K. T. Compton, Rev. Mod. Phys. 3, 191 (1931).

79. L. P. Bradley and T. H. Martin, unpublished.

80. S. Singer, Digest of Technical Papers, Conf. on Laser and Engineering Applications (May 28-30, 1975), p. 44.

81. G. Loda et al., Physics International Company Rept. PIFR 526 (May 1972).

82. J. C. Martin, private communication.

83. H. T. Powell, private communication.

84. L. Jedynak et al., J. Vac. Sci. Technol. 11, 472 (1974).

85. J. G. Trump, in Proc. 3rd Int. Symp. Discharge and Electron Insulation in Vacuum (Sept. 1968), p. 235.

86. J. C. Martin, private communication.

87. L. G. Schlitt, Bull. Am. Phys. Soc. 19, 871 (1974).

88. J. B. Gerardo, Digest of Technical Papers, Conf. on Laser and Engineering Applications (May 28-30, 1975), p. 56.

89. The Taylor Manual, T. B. Brown, Ed. (Addison Wesley, 1959).

90. W. B. Herrmannsfeldt, Stanford Linear Accelerator Center, Report 166 (Sept. 1973).

91. L. P. Bradley, Lawrence Livermore Laboratory, Laser Fusion Program Report (Jan.-June 1973), p. 112.

92. L. P. Bradley et al., in Proc. 11th Symp. on Electron, Ion, and Laser Beam Technology (Boulder, Colorado, May 12-14, 1971).

93. B. W. Schumacher, Westinghouse, Research Rept. 71-1C2-EWELD-P1 (March 1971).

94. F. A. Fitch, IEEE Trans. Nucl. Sci. 18, 190 (Aug. 1971).

95. N. W. Harris and H. J. Hilde, in Proc. 15th Symp. Electron, Ion, and Laser Beam Tech. (Colorado Springs, Colorado, May 21-23, 1975).

96. I. A. Abramyan, Nucl. Instrum. Methods 59, 22 (1968).

97. J. G. Trump et al., High Voltage Technology Seminar, Boston, Mass, 1969 (IPC, Mass., 1969).

98. R. A. Fitch and V. T. S. Howell, IEEI 111, 849 (1964).

99. K. R. Prestwich and D. L. Johnson, IEEE Trans. Nucl. Sci. NS16, 64 (1969).

100. R. Fitch, private communication.

101. T. H. Martin, private communication.

102. K. B. Riepe and R. E. Stapleton, in Proc. 5th Symp. Engineering Problems of Fusion (Princeton, N.J., Nov. 5-9, 1973), p. 626.

103. J. R. Uglan, IEEI Trans. Nucl. Sic. 1026 (1975).

104. G. Breit and M. A. Tuve, Nature 121, 535 (1928).

105. T. H. Martin, IEEE Trans. Nucl. Sci. NS18, 104 (1971).

106. G. Brautti et al., IEEI Trans. Nucl. Sci. NS20, 286 (1973); and C. R. J. Hoffmann, Rev. Sci. Instrum. 46, 1 (1975).

107. J. C. Martin, P. D. Champney, and D. A. Hammer, Construction Methods of a Martin High Voltage Transformer, unpublished.

108. G. J. Rohwein, IEEE NS22, 1013 (1975).

109. C. Edwards, M. D. Hutchinson, J. C. Martin, and T. H. Storr, Atomic Weapons Research Establishment Research Note, SSWA/JCM/755/99.

110. J. Harrison et al., in Proc. 5th Symp. Engineering Problems of Fusion Research (Princeton, N.J., Nov. 5-9, 1973), p. 640.

111. K. R. Prestwich, IEEE Trans. Nucl. Sci. 22, 975 (1975).

112. D. W. Forrester, in Proc. 15th Symp. Electron, Ion, and Laser Beam Tech. (Colorado Springs, Colorado, May 21-23, 1975).

113. G. Yonas, in Proc. APS Topical Conf. Physics Opportunities in Energy Problems (Chicago, Illinois, Feb. 4-7, 1974).

114. J. C. Martin, Nanosecond Pulse Techniques, Atomic Weapons Research Establishment Research Notes, SSWA-JCM-704-49.

115. M. E. Valkenburg, Network Analysis, (Prentice Hall, 1955).

116. Blumlein, U.S. Patent 589127 (Oct. 1941).

117. H. T. Milde and H. C. Stevens, Laser Focus (Nov. 1974).

118. H. G. Ahlstrom et al , Appl. Phys. Lett. 21, 492 (1972).

119. K. Manes et al., Lawrence Livermore Laboratory Rept. UCRL-51729 (1975).

120. E. A. Guilleman, M.I.T. Radiation Laboratory Rept. 45 (Oct. 16, 1944).

121. G. N. Glasoe and J. V. Lebacqz, Pulse Generators (M.I.T. Press, Mass., 1948).

122. S. Seshv and N. Balabanian, Linear Network Analysis (Wiley, 1959).

123. R. K. Parker and M. Ury, IEEE Trans. Nucl. Sci. NS22, 983 (1975).

124. G. B. Frazier, in Proc. 15th Symp. Electron, Ion, and Laser Beam Technology (Colorado Springs, Colorado, May 21-23, 1975), to be published.

125. A. S. Denholm et al., Air Force Weapons Laboratory, Rept. TR 72-88 (1973).

126. F. B. A. Früngel, High Speed Pulse Technology, Vol. 1, II (Academic Press, 1965).

127. Lawrence Livermore Laboratory, Laser Program Annual Rept. (1974).

128. S. C. Fultz et al., IEEE Trans. Nucl. Sci. NS18, 535 (1971).

129. H. T. Powell and J. R. Murray, private communication.

130. J. B. Trenholme and K. R. Manes, Lawrence Livermore Laboratory, Rept. UCRL-51410 (1972).

131. G. Dzakowic et al., Lawrence Livermore Laboratory, Rept. UCID-16755.

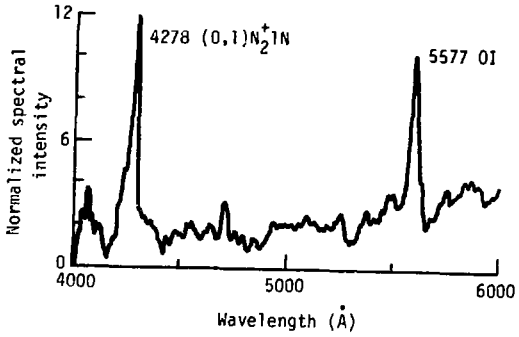

Fig. 1. Spectra of artificial e beam produced aurora in the ionosphere.

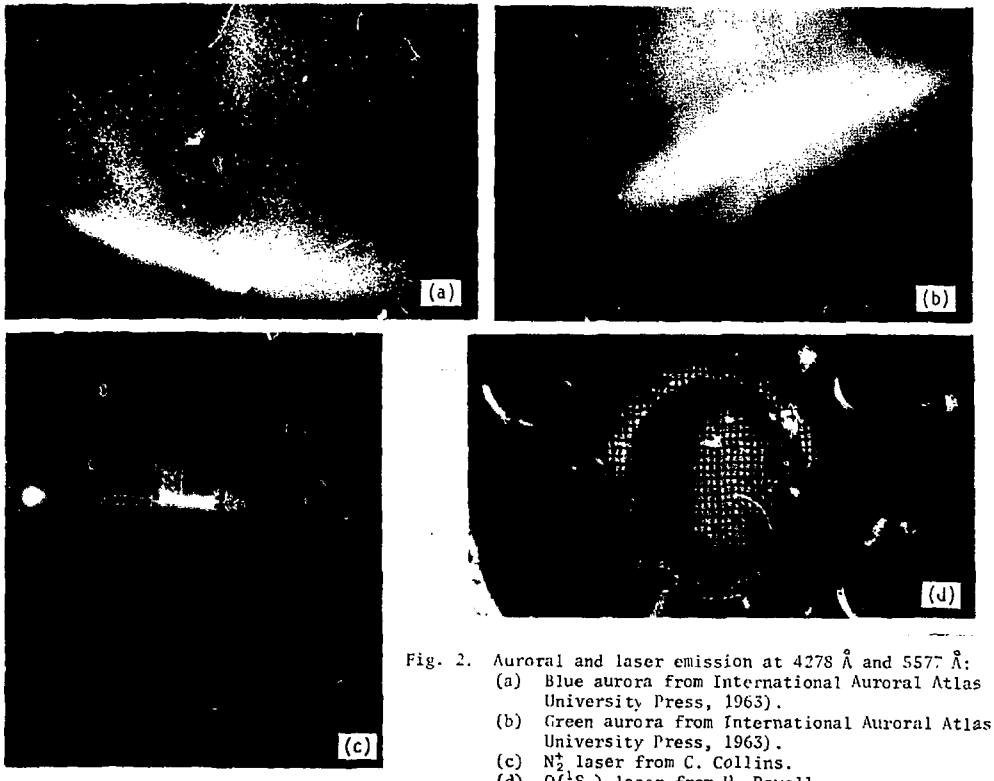

Fig. 2. Auroral and laser emission at 4278 Å and 5577 Å:
(a) Blue aurora from International Auroral Atlas (Edinburgh University Press, 1963).
(b) Green aurora from International Auroral Atlas (Edinburgh University Press, 1963).
(c) N_2^+ laser from C. Collins.
(d) $O(^1S_0)$ laser from H. Powell.

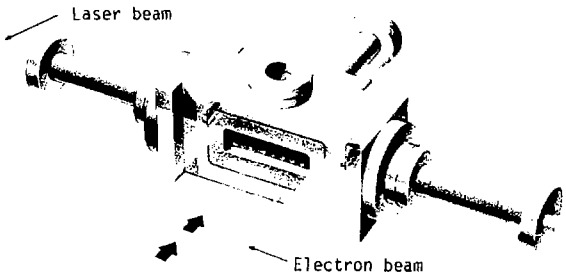

Fig. 3. Typical transverse e-beam pumped laser.

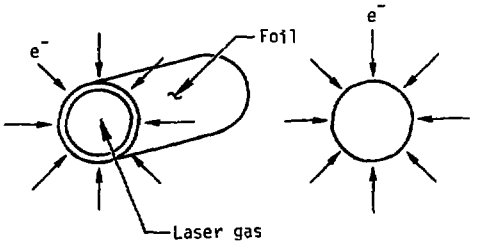

(a)

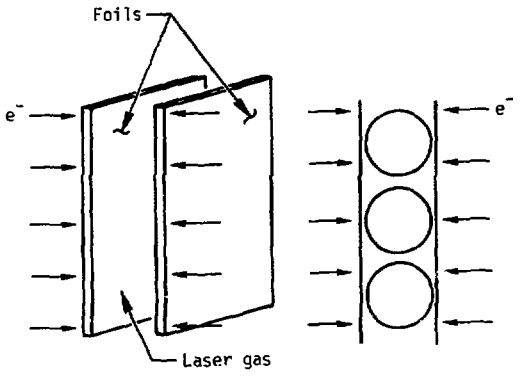

(b)

Fig. 4. Transverse e-beam pump configurations: (a) Cylindrical geometry, (b) slab geometry.

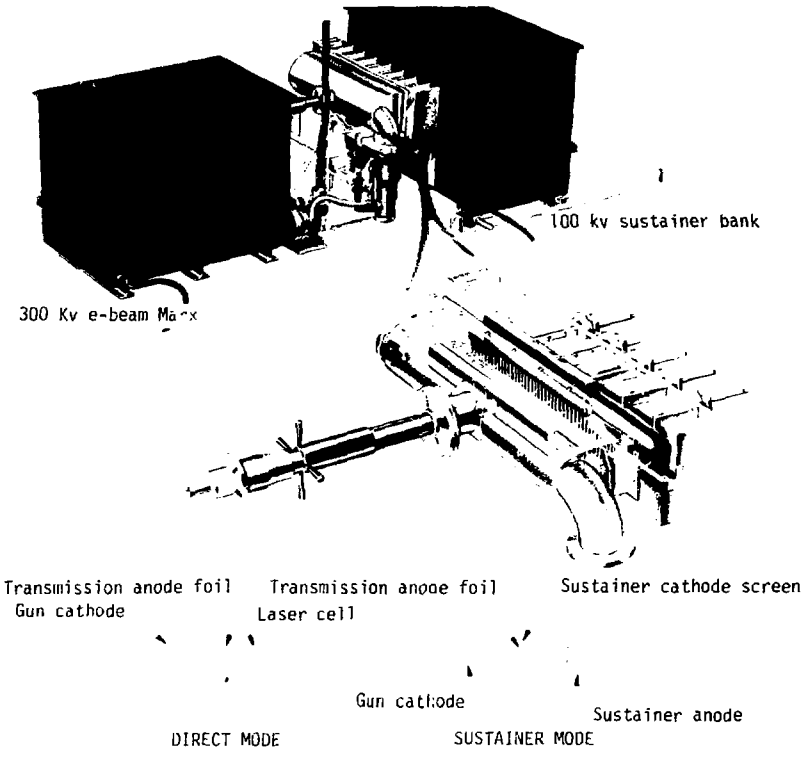

Fig. 5. EB 300 electron beam laser source.

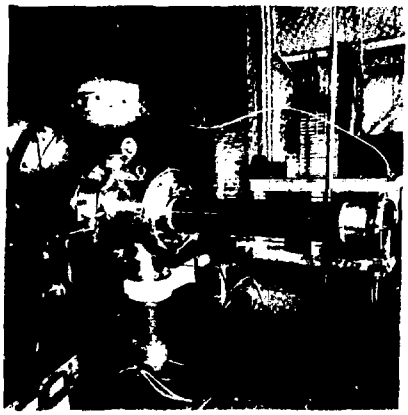

Fig. 6. Axial e-beam pump with B_z guide field (HF laser at Los Alamos Scientific Laboratory).

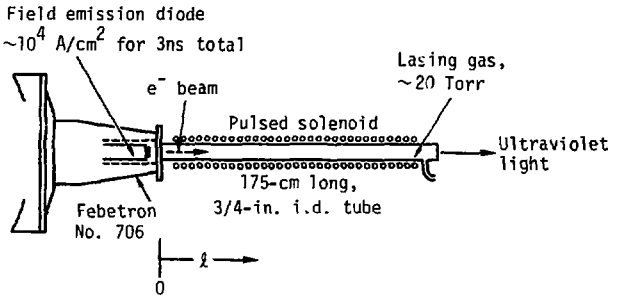

Fig. 7. E-beam pumped N_2 laser (from Dreyfus and Hodgson. IBM Research Rept. RC 3619, Nov. 18, 1971).

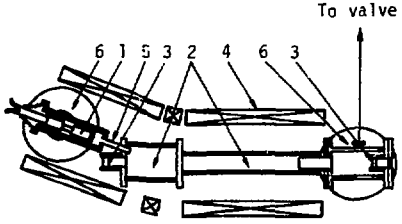

1. Electron run
2. Plasma chamber
3. Mirror
4. Solenoid
5. Pressure-drop tube
6. Diffusion pumps
7. Gas-inlet system

Fig. 8. E-beam pumped Ar^+ laser (from Yu. V. Tkach, Ya. B. Faynberg, and L. I. Bolotin, Pis'ma v Zh. Eksp. Theor. Fiz., 6, 956 (1967)). Diagram of setup: (1) electron gun, (2) plasma chamber, (3) mirror, (4) solenoid, (5) pressure-drop tube, (6) diffusion pumps, and (7) gas-inlet system.

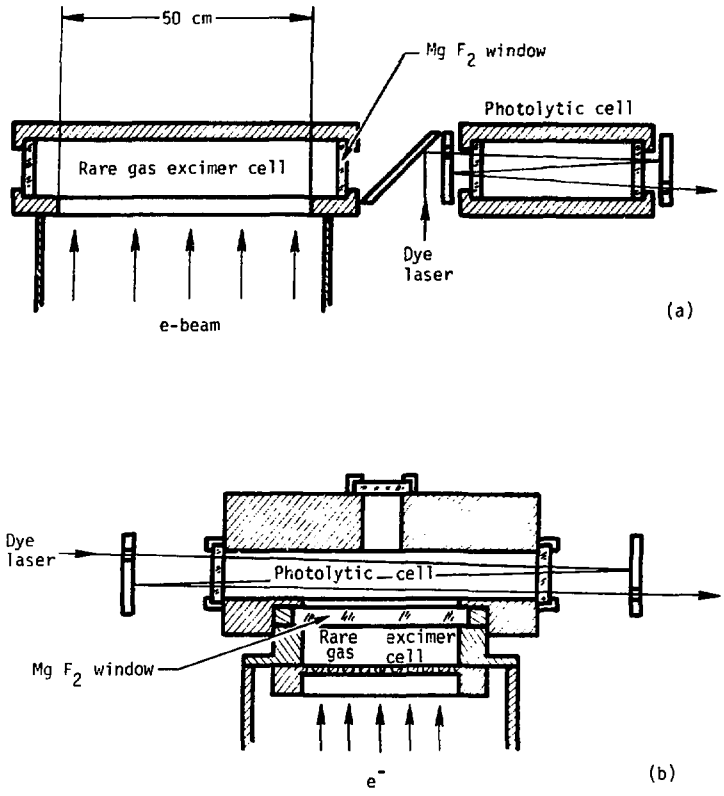

Fig. 9. Photolytic transfer configurations: (a) laser, (b) fluorescent.

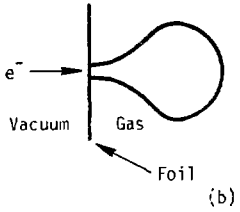

Fig. 10. Electron beamlet injected into gas: (a) photograph of fluorescence, (b) sketch of geometry.

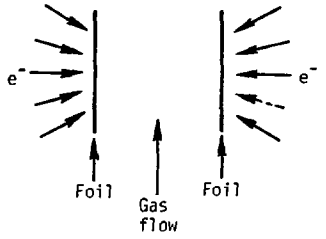

Fig. 11. Convergent two-side e-beam injection into cell.

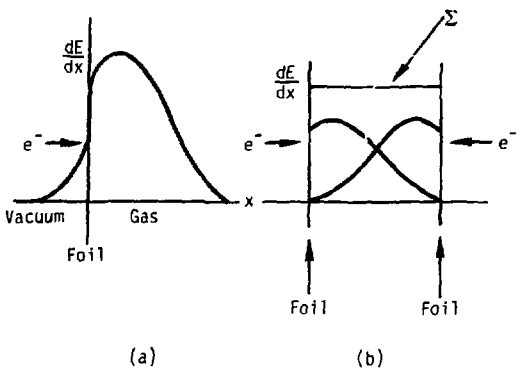

Fig. 12. Energy deposition profile for e beam injected into gas: (a) one-side injection, (b) two-side injection.

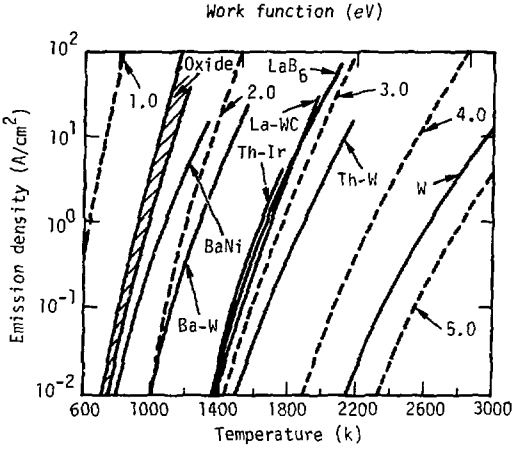

Fig. 13. Saturated emission-current density versus temperature for several types of cathodes (solid lines). The Ba-W line is representative of the impregnated tungsten cathode. The dashed lines are drawn for constant values of work function (from Amboss, see Ref. 49).

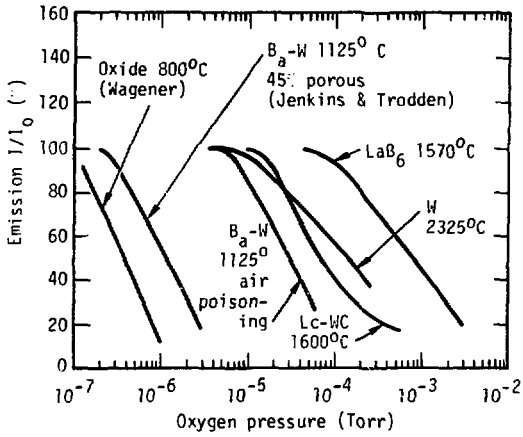

Fig. 14. Reduction in emission of various cathodes as a function of oxygen pressure. Also shown is the air poisoning characteristic of a Ba-W cathode at 1125 K (from Amboss, Ref. 49).

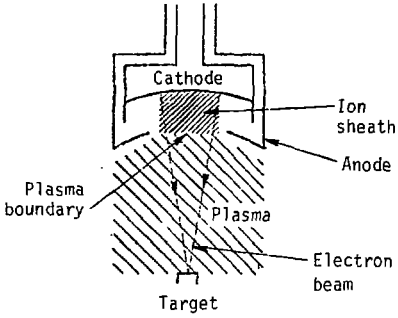

Fig. 15. Glow diode gun (from Isaacs, Electron. Lett. 3, 542 (1967)).

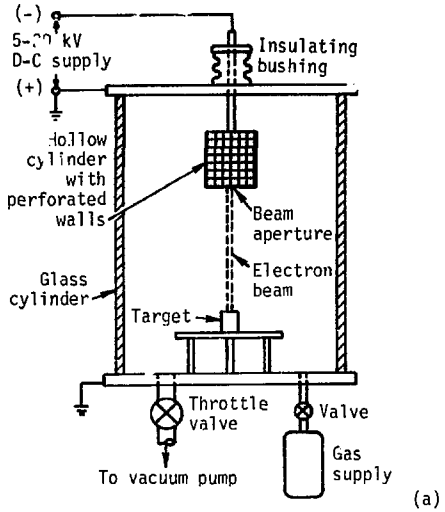

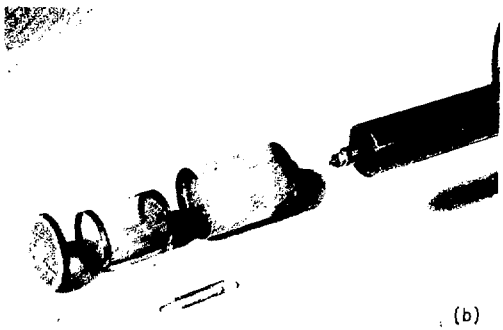

Fig. 16. Grid-controlled glow gun (from Cocca and Stauffer, in Proc. 5th Electron Beam Symp. (Boston, Mass., March 28-29, 1963)): (a) schematic of experimental assembly, (b) exploded view of grid-controlled cathode assembly.

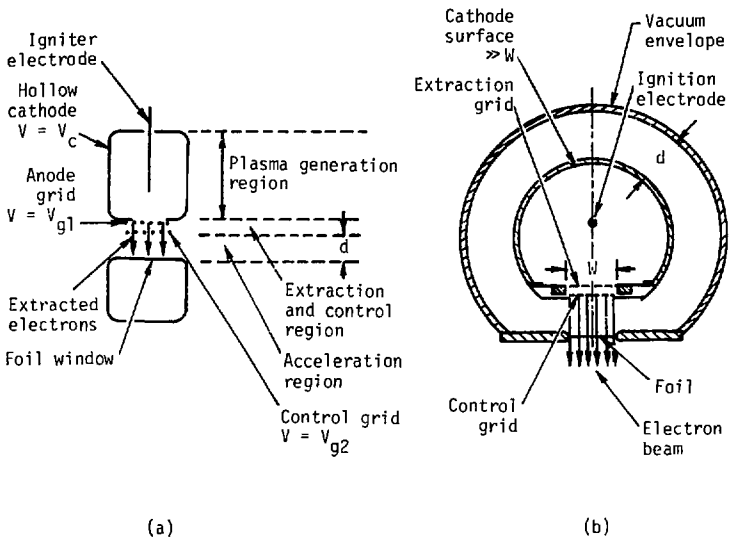

Fig. 17. Plasma cathode electron gun (from Bayless and Hughs, Research Laboratory Rept. N00014-72-6-0496): (a) schematic of a plasma cathode electron gun, (b) schematic cross section of a cylindrical high-voltage plasma-gun design.

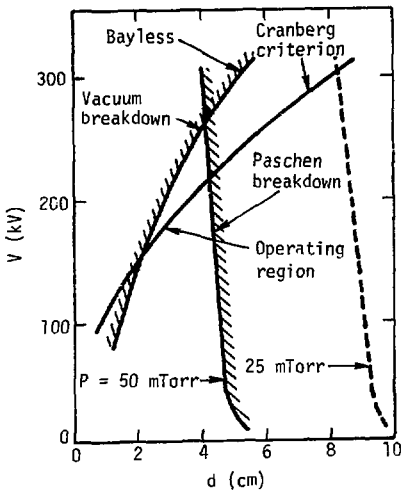

Fig. 18. Low-pressure breakdown characteristics for p = 25 and 50 mTorr (from Bayless and Hughs, Research Laboratory Rept. N00014-72-C-0496).

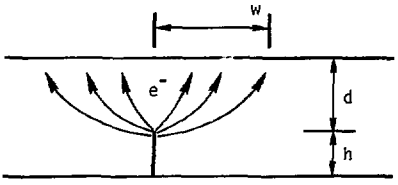

Fig. 19. Geometry for single blade cathode.

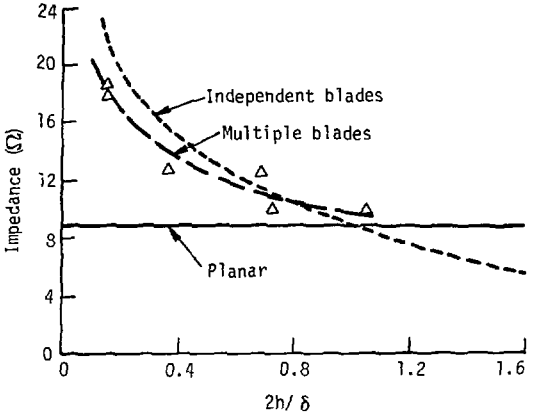

Fig. 20. Experimental blade impedance as function of $2h/\delta$ for multiple blades, and theoretical comparison assuming independent blades or planar limit where h is blade height and δ is blade separation.

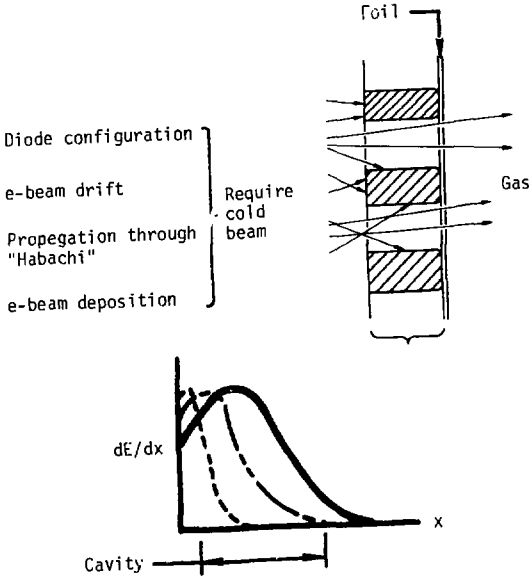

Fig. 21. E-beam source characteristics.

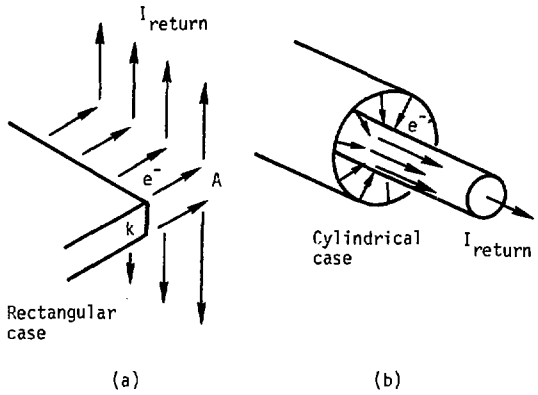

Fig. 22. Path of current flow for two e-beam pump geometries: (a) rectangular case, (b) cylindrical case.

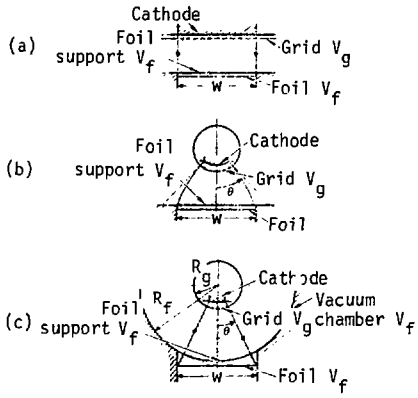

Fig. 23. Electron optical schemes for producing large area flows (from Amboss, Ref. 49): (a) planar flow gun, (b) planar-cylindrical flow gun, (c) cylindrical flow gun.

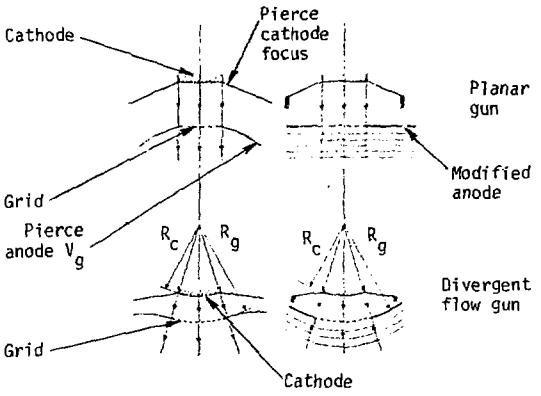

Fig. 24. Theoretical Pierce electrodes for planar and practical divergent cylindrical flows (from Amboss, Ref. 49).

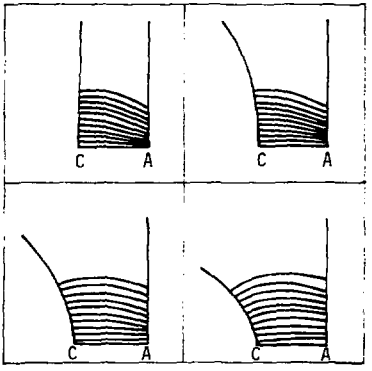

Fig. 25. Effect on electron trajectories of shaping the cathode (from Schlitt, Lawrence Livermore Laboratory, Lasar Program Annual Rept. (1974)).

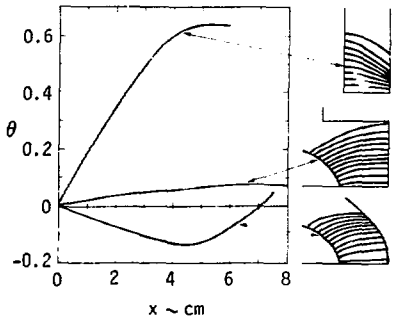

Fig. 26. Combined effect of anode and cathode grading (from Schlitt, Lawrence Livermore Laboratory, Laser Program Annual Rept. (1974)).

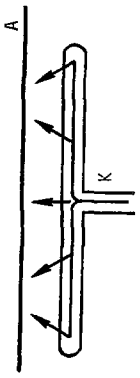

Fig. 27. Electron current flow and consequent trajectory distortion in geometry of Fig. 5.

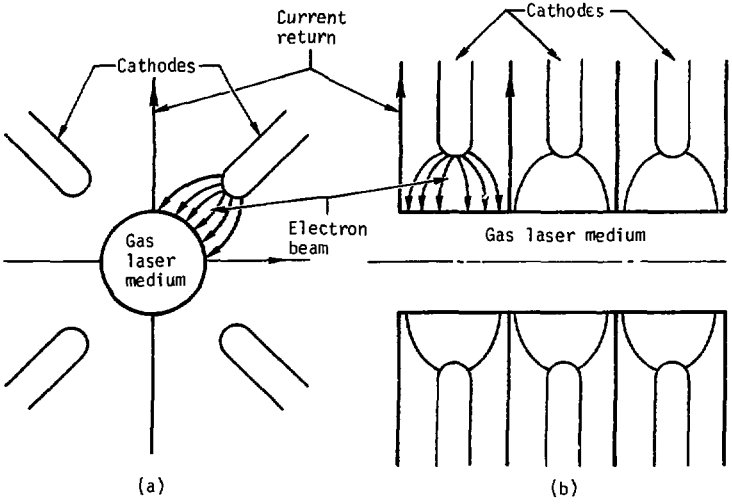

Fig. 28. Diode modularization geometries (from Schlitt, Ref. 45): (a) bar cathode, (b) hoop cathode.

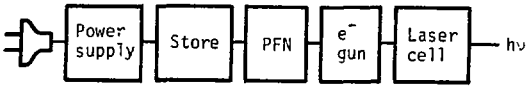

Fig. 29. Block diagram of energy flow from plug to laser beam.

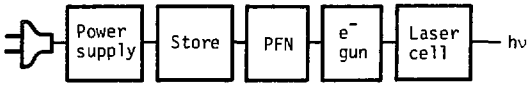

Fig. 29. Block diagram of energy flow from plug to laser beam.

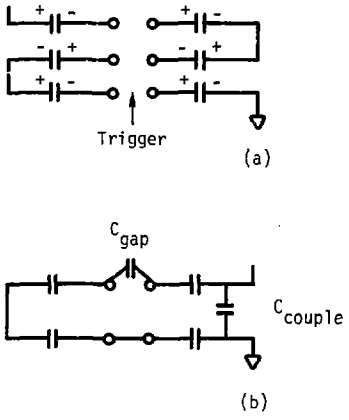

Fig. 30. Marx triggering: (a) schematic of Marx with first stage triggered, (b) coupling when first gap closes.

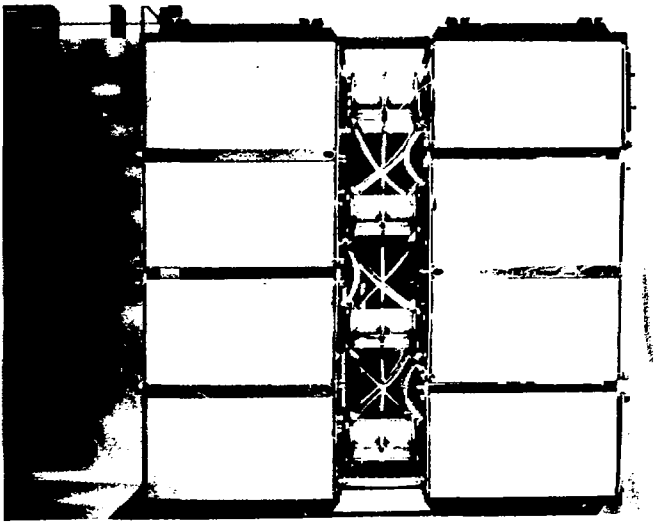

Fig. 31. Four stages of hydra Marx.

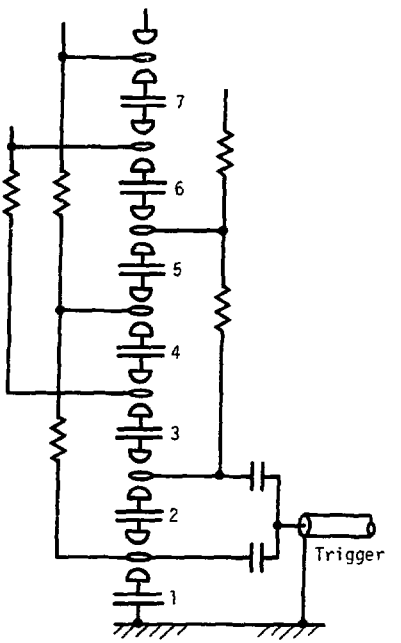

Fig. 32. Marx with m = 2 triggering.

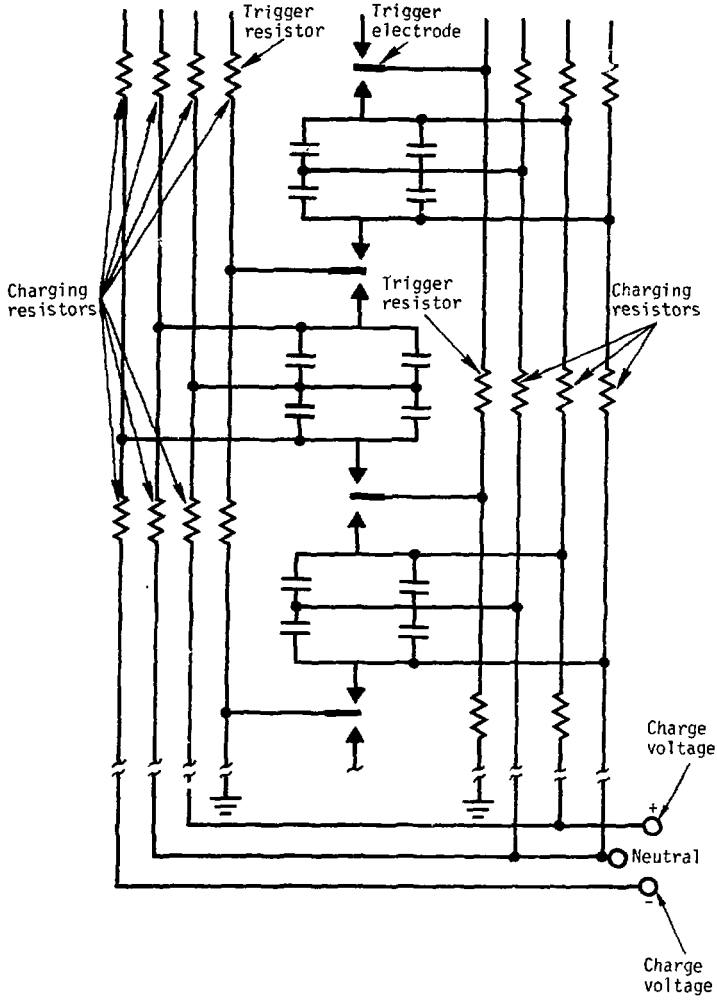

Fig. 33. Basic Marx circuit: Pulspak 8000 (from T. Naff, Pulsar).

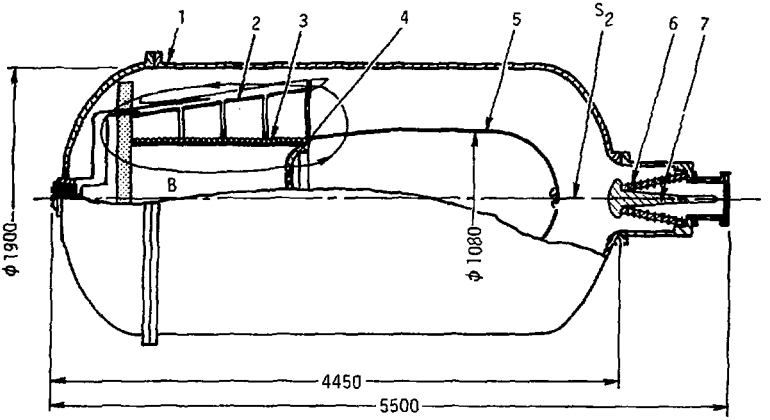

Construction scheme of the transformer accelerator (from Ref. 96)

1. Tank
2. Primary winding
3. Secondary winding
4. Shield
5. High-voltage electrode
6. Accelerating tube
7. Cathode
B. Transformer magnetic field
S_2. Triggered gap

Fig. 34. Construction scheme of the transformer accelerator (from Ref. 96): (1) tank, (2) primary winding, (3) secondary winding, (4) shield, (5) high-voltage electrode, (6) accelerating tube, (7) cathode, (B) transformer magnetic field, and (S_2) triggered gap.

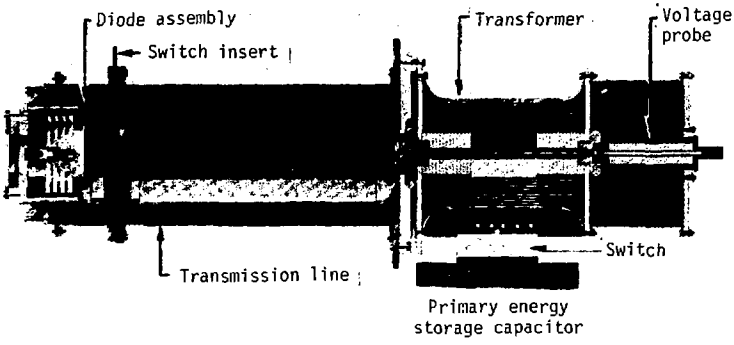

Fig. 35. Transformer driven PFL and diode (from Ref. 108).

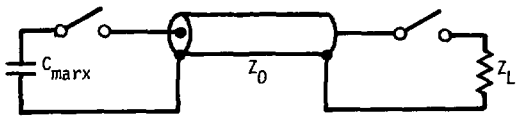

Fig. 36. Basic PFL circuit.

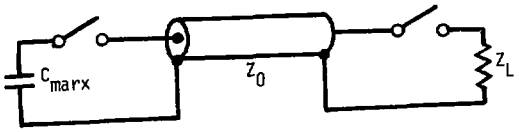

Fig. 36. Basic PFL circuit.

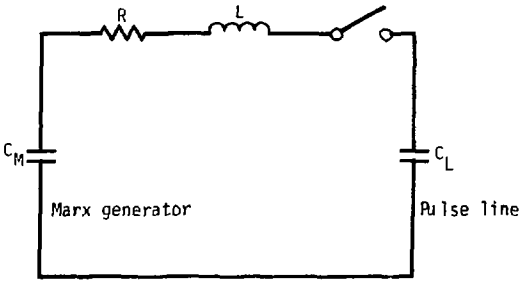

Fig. 37. Simple model for pulse line charging.

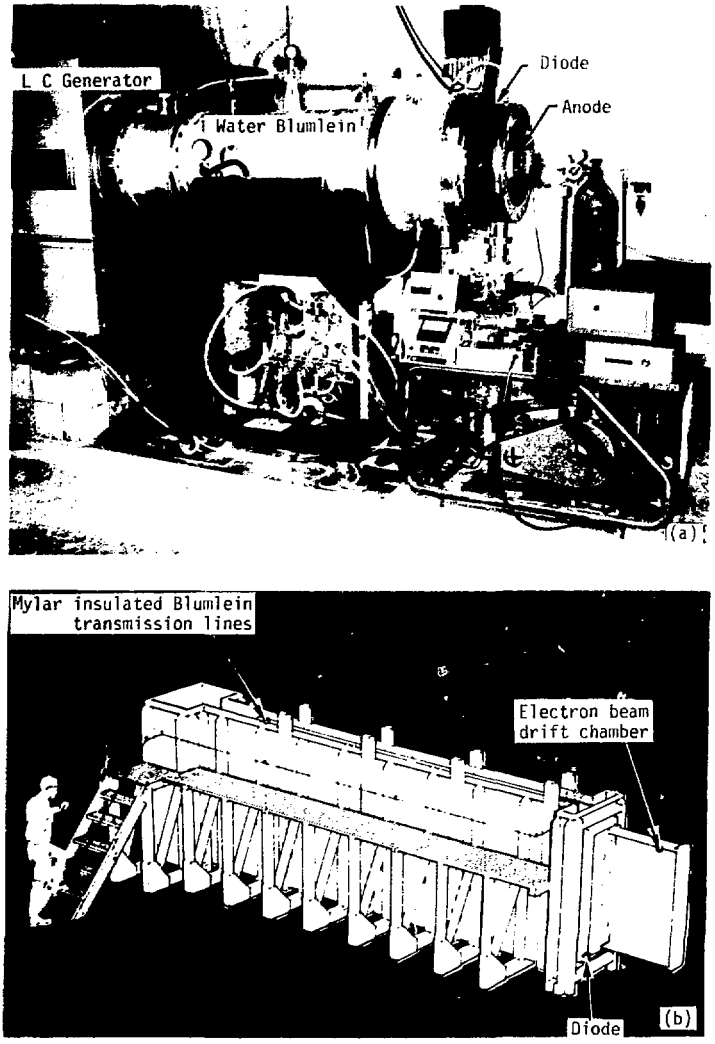

Fig. 38. Blumlein geometries: (a) coaxial 700 kV (from Shipman and Ury, NRL), (b) flat plate 300 kV (from Prestwich, SLA).

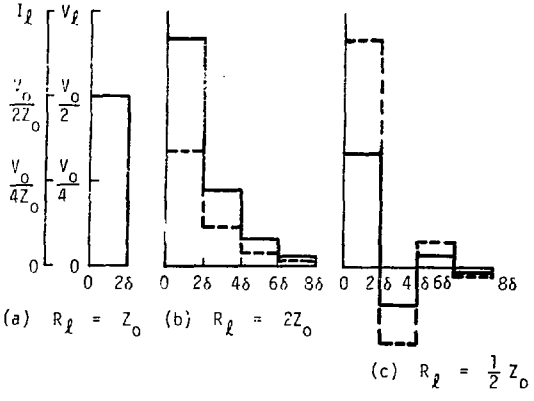

Fig. 39. Current and voltage pulses for a lossless transmission line discharging into a resistance load. The solid and broken lines represent the voltage and current pulses, respectively (from Ref. 121).

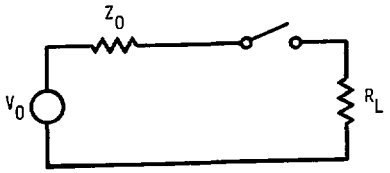

Fig. 40. Thevinin equivalent circuit of PFL during discharge.

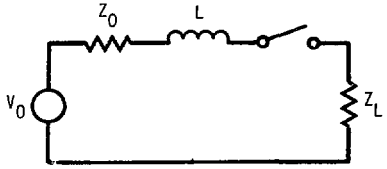

Fig. 41. Equivalent circuit of PFL during discharge including inductance.

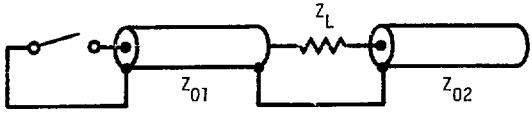

Fig. 42. Blumlein circuit.

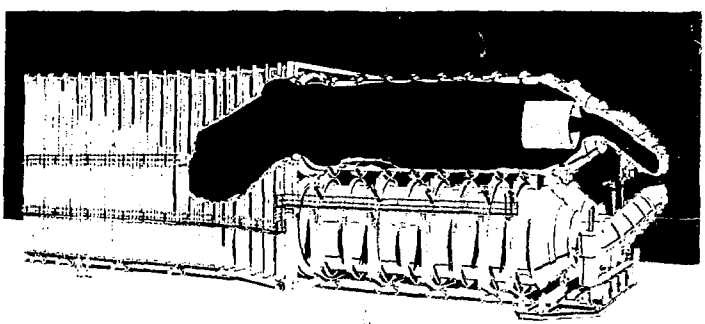

Fig. 43. Folded Blumlein: Aurora (from Ref. 118).

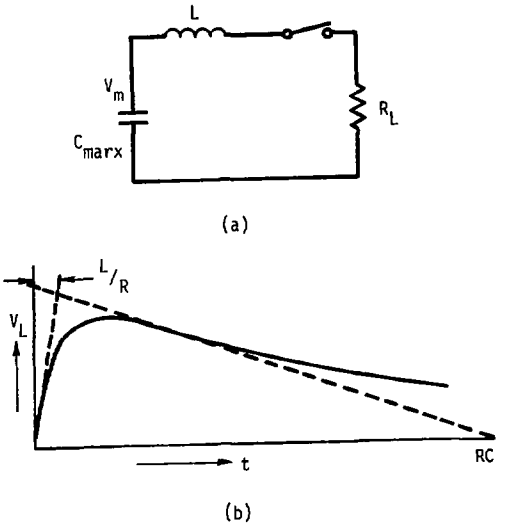

Fig. 44. Marx gun: (a) equivalent circuit, (b) load voltage waveform.

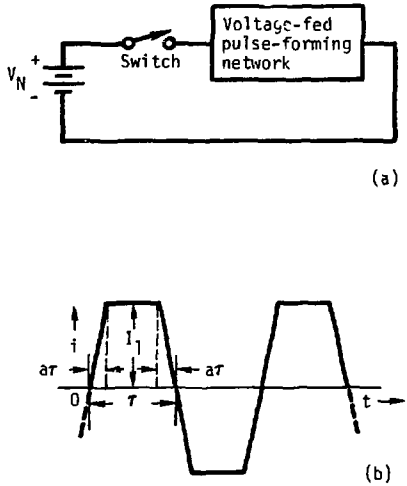

Fig. 45. Voltage-fed pulse forming network (from Ref. 121): (a) circuit for producing a specified steady-state alternating-current wave similar to the desired single-pulse shape, (b) trapezoidal alternating-current wave.

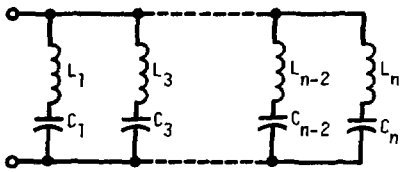

Fig. 46. Form of voltage-fed network derived by Fourier-series analysis of a specified-alternating-current waveform (from Ref. 121).

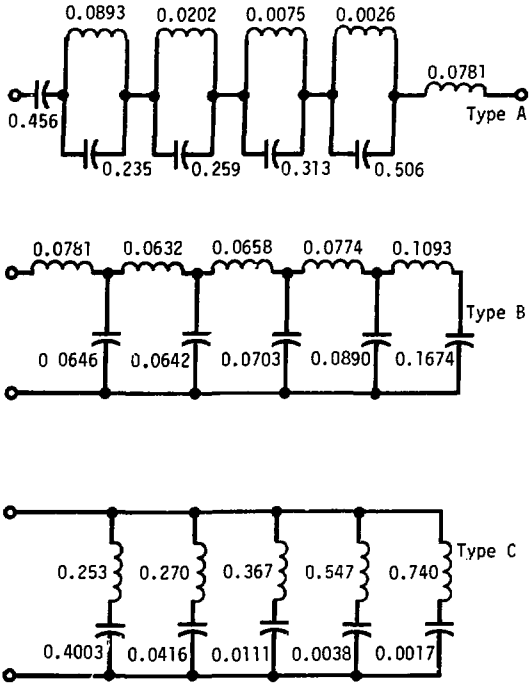

Fig. 47. Guilleman circuits (from Ref. 120).

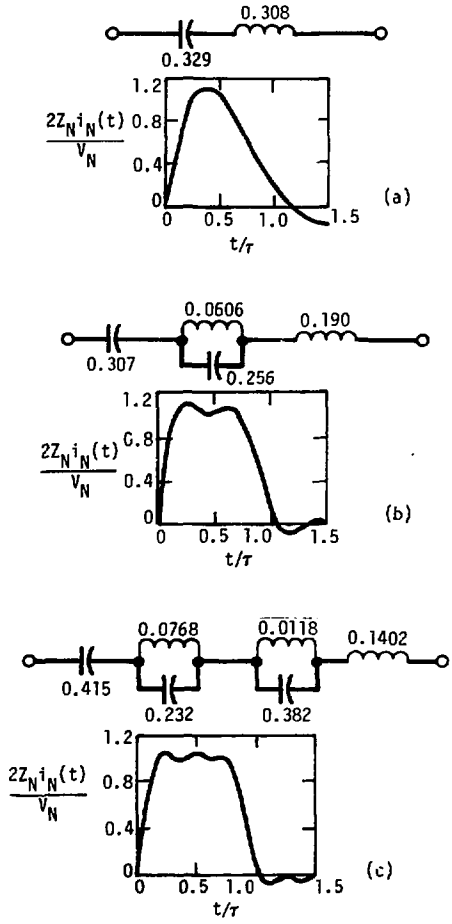

Fig. 48. Waveforms for one-, two-, and three-section type-A circuits (from Ref. 121). Multiply the inductance by $Z_{N\tau}$ and the capacitances by τ/Z_N. The inductances are in henrys and the capacitances in farads if pulse duration τ is expressed in seconds and network impedance Z_N in ohms: (a) one section a = 0.5, (b) two section a = 0.33, (c) three section a = 0.25, with pulse shapes calculated for a,b,c.

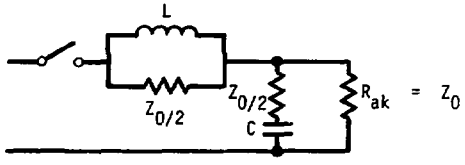

Fig. 49. Compensating circuit (from Riepe, Ref. 102).

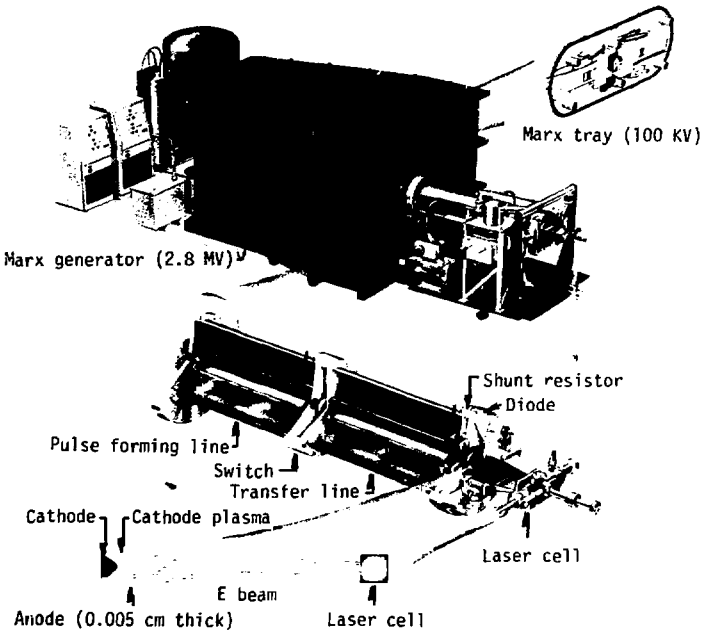

Fig. 50. 1 MeV, 100 kA MEG electron beam generator.

Fig. 51. MEG I with laser cell.

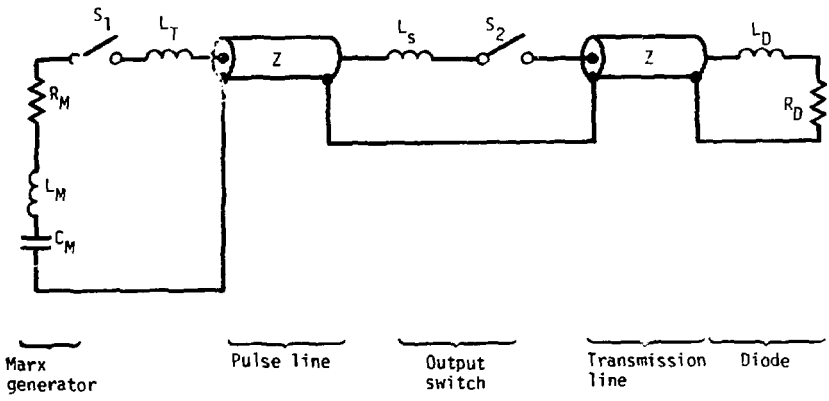

Fig. 52. Simplified equivalent circuit of MEG I, where C_M = Marx capacitance, L_M = Marx inductance, R_M = Marx resistance, L_T = transfer inductance, L_S = output switch inductance, L_D = diode inductance, R_D = diode impedance, S_1 = effective Marx switch, S_2 = output switch, Z = characteristic impedance.

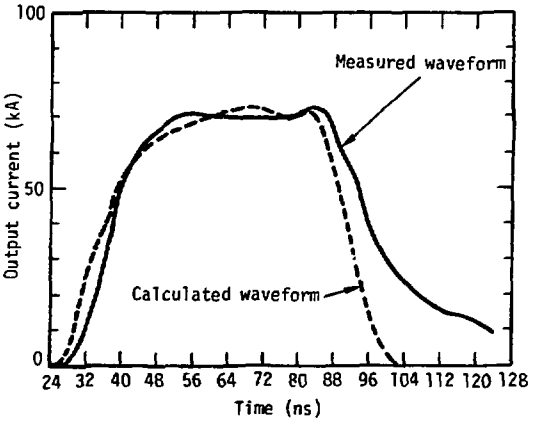

Fig. 53. Calculated and measured current waveforms of MEG I.

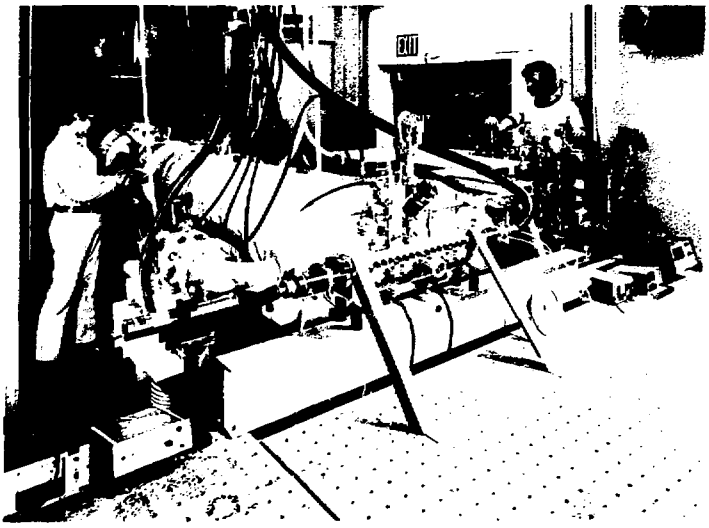

Fig. 54. Powell and Booth adjusting MEG II laser experiment.

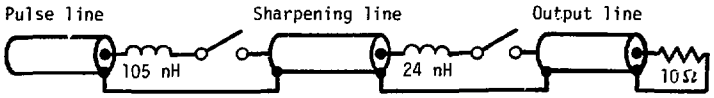

Fig. 55. Transmission line model used for computer simulation of MEG II.

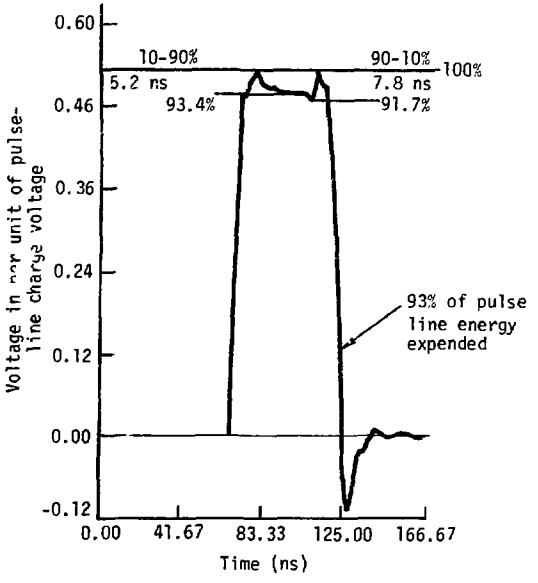

Fig. 56. Diode voltage waveform with four active channels in sharpening gap for MEG II.

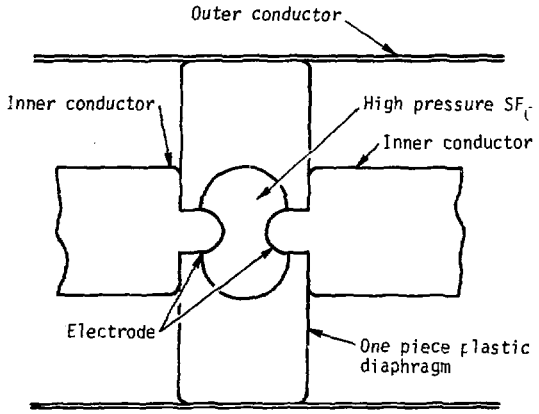

Fig. 57. High-pressure diaphram switch.

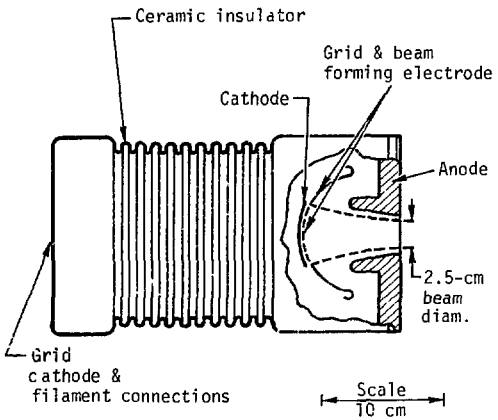

Fig. 58. LAMP gun outline.

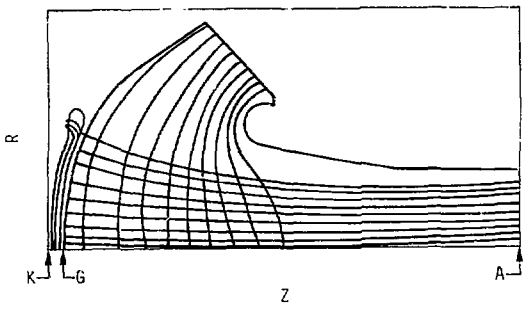

Fig. 59. LAMP electron trajectories and equipotentials.

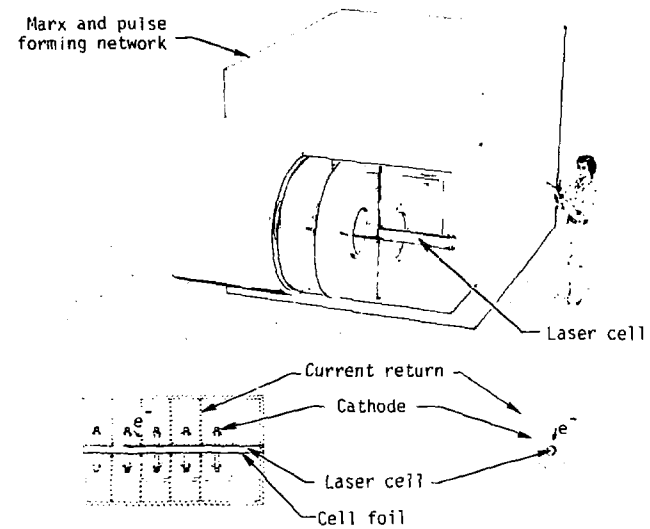

Fig. 60. MEG III visible power amplifier.

NOTICE

"This report was prepared as an account of work sponsored by the United States Government. Neither the United States nor the United States Energy Research & Development Administration, nor any of their employees, nor any of their contractors, subcontractors, or their employees, makes any warranty, express or implied, or assumes any legal liability or responsibility for the accuracy, completeness or usefulness of any information, apparatus, product or process disclosed, or represents that its use would not infringe privately-owned rights."

JRH/lt/1a